J. Fluid Mech. (2022), *vol*. 944, A15, doi:10.1017/jfm.2022.468

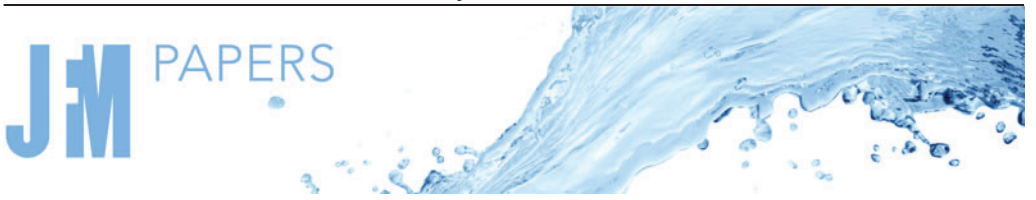

Spontaneous and explicit symmetry breaking of thermoacoustic eigenmodes in imperfect annular geometries

Thomas Indlekofer[1],†, **Abel Faure-Beaulieu**[2], **James R. Dawson**[1] and **Nicolas Noiray**[2],†

[1]Department of Energy and Process Engineering, Norwegian University of Science and Technology, Trondheim, N-7491, Norway

[2]CAPS Laboratory, Department of Mechanical and Process Engineering, ETH Zürich, Zürich 8092, Switzerland

(Received 17 November 2021; revised 24 May 2022; accepted 24 May 2022)

This article deals with the symmetry breaking of azimuthal thermoacoustic modes in annular combustors. Using a nominally symmetric annular combustor, we present experimental evidence of a predicted spontaneous reflectional symmetry breaking, and also an unexpected explicit rotational symmetry breaking in the neighbourhood of the Hopf bifurcation which separates linearly stable azimuthal thermoacoustic modes from self-oscillating modes. We derive and solve a multidimensional Fokker–Planck equation to unravel a unified picture of the phase space topology. We demonstrate that symmetric probability density functions of the thermoacoustic state vector are elusive, because the effect of asymmetries, even imperceptible ones, is magnified close to the bifurcation. This conclusion implies that the thermoacoustic oscillations of azimuthal modes in real combustors will systematically exhibit a statistically dominant orientation of the mode in the vicinity of the Hopf bifurcation.

Key words: combustion, acoustics, nonlinear dynamical systems

1. Introduction

Symmetry breaking in systems where waves propagate along closed loops or spheres occur in a wide variety of physical problems. Examples range from Bose–Einstein condensates in toroidal traps (e.g. Marti, Olf & Stamper-Kurn 2015), whispering gallery modes in optomechanical resonators (e.g. Shen *et al.* 2016), counter-propagating modes in optical ring cavities (e.g. Megyeri *et al.* 2018), non-reciprocal acoustic circulators

† Email addresses for correspondence: thomas.indlekofer@sintef.no, noirayn@ethz.ch

(Fleury *et al.* 2014), intrinsic rotation in tokamak plasmas (Rice *et al.* 2011), to sporadic reversal in direction of planetary dynamo waves (e.g. Pétrélis *et al.* 2009) and non-radial stellar pulsations (Aerts 2021). Symmetry breaking is also ubiquitous in fluid mechanics (Crawford & Knobloch 1991), for example in von-Kármán swirling flows with counter-rotating toroidal vortices investigated by López-Caballero & Burguete (2013) and Faranda *et al.* (2017). Recently, symmetry breaking was observed for azimuthal thermoacoustic modes in annular combustors typically found in jet engines or power generation gas turbines. First described by Rayleigh (1878), thermoacoustic instabilities that arise from a constructive coupling between the acoustic field and the heat-release-rate fluctuations of the flames lead to damaging vibrations (Lieuwen 2012; Poinsot 2017).

Azimuthal thermoacoustic modes have been investigated in real engines (e.g. Seume *et al.* 1998; Krebs *et al.* 2002; Noiray & Schuermans 2013*b*), laboratory experiments (e.g. Worth & Dawson 2013; Bourgouin *et al.* 2015*a*; Worth & Dawson 2017; Fang *et al.* 2021; Singh *et al.* 2021) and numerical simulations (Wolf *et al.* 2012). Over the last decade, the dynamic nature of these modes has received significant attention, as shown in the review article from Bauerheim, Nicoud & Poinsot (2016), and the following classification has been established: standing modes, whose nodal line direction remains constant or slowly drifts around the annular chamber, spinning modes, whose nodal line spins at the speed of sound, or a combination of both referred to as mixed modes can exist. Slanted modes resulting from the synchronization of a pure longitudinal mode and an azimuthal mode with very close eigenfrequencies have been discovered by Bourgouin *et al.* (2015*b*), modelled by Moeck *et al.* (2019) and further scrutinized by Prieur *et al.* (2017) and Aguilar *et al.* (2021). Very recently, Indlekofer *et al.* (2021) and Faure-Beaulieu *et al.* (2021*b*) reported and modelled beating modes, whose spinning direction changes periodically in synchrony with the direction of the standing wave component's nodal line.

Several experimental and theoretical studies focused on the effects of combustor asymmetries and azimuthal mean flow upon the dynamics of azimuthal modes (Noiray, Bothien & Schuermans 2011; Bauerheim *et al.* 2014; Berger *et al.* 2018; Mensah *et al.* 2019; Humbert *et al.* 2021; Kim *et al.* 2022). Reduced-order models were developed to explain some of the experimental observations (Evesque, Polifke & Pankiewitz 2003; Schuermans, Paschereit & Monkewitz 2006; Ghirardo, Juniper & Moeck 2016; Magri *et al.* 2016; Orchini, Mensah & Moeck 2019; Yang, Laera & Morgans 2019*a*; Buschmann, Mensah & Moeck 2020; Li *et al.* 2020*b*; Fournier *et al.* 2021), and to predict linear stability for combustor design optimization and instability control (Morgans & Stow 2007; Yang *et al.* 2019*b*; Li, Morgans & Yang 2020*a*; Laurent, Badhe & Nicoud 2021). Recently, a quaternion-based ansatz for describing the acoustic field from Ghirardo & Bothien (2018) was combined with the wave equation by Faure-Beaulieu & Noiray (2020) to describe an ideal annular combustor, unifying previous modelling approaches. The latter theoretical article first considers the effects of time delayed flame response, asymmetries and mean azimuthal flow in a deterministic framework. Second, it investigates theoretically the effect of additive stochastic forcing from the turbulent combustion noise that is inherent to practical combustors. However, this reference does not present the Fokker–Planck equation describing the probability density function of the thermoacoustic state, and does not include experimental results.

The present paper deals with explicit and spontaneous breaking of rotational and reflectional symmetries of the thermoacoustic dynamics. Let us now clarify the meaning of these different types of symmetry breaking and the associated available experimental and theoretical knowledge.

Explicit rotational symmetry breaking – corresponds to situations where mixed or standing thermoacoustic modes exhibit one or several preferential orientations, which are consistently repeatable when the annular combustor is re-ignited and set to the same operating condition. These preferred mode orientations originate from rotational asymmetries of the annular configuration. When the turbulent combustion noise is significant, such preferred orientation of the mode can be identified from sufficiently long observation of the thermoacoustic dynamics at a stationary operating condition. Dawson & Worth (2013) and Aguilar *et al.* (2021) investigated this type of symmetry breaking by means of various rotationally asymmetric annular configurations, and Noiray *et al.* (2011) showed that rotational resistive acoustic asymmetries cause this type of symmetry breaking of the thermoacoustic dynamics.

Explicit reflectional symmetry breaking – corresponds to the preference of mixed or spinning modes for the clockwise (CW) or the counterclockwise (CCW) spinning direction. When the natural stochastic forcing from the turbulent combustion noise is negligible, this preference can be found by performing a series of re-ignitions at the considered operating condition and collect the statistics of CW vs CCW stable limit cycles. When the noise is significant at a given stationary operating condition, the mixed mode sporadically change its spinning direction and the preference for CW or CCW spinning can be deduced from sufficiently long observations. This symmetry breaking of the thermoacoustic dynamics originates from a reflectional asymmetry of the annular configuration, e.g. in presence of a mean azimuthal flow (Worth & Dawson 2013; Faure-Beaulieu & Noiray 2020; Ghirardo *et al.* 2021), or from rotational resistive and reactive asymmetries with different orientations (Faure-Beaulieu *et al.* 2021*b*). This last reference presents experiments performed with the same combustor as in the present work, but at different operating conditions.

Spontaneous reflectional symmetry breaking – corresponds to situations for which, although the annular configuration is symmetric, the quasi-steady increase of a system parameter leads, beyond a certain threshold, to a loss of reflectional symmetry of the thermoacoustic dynamics. This phenomenon has been investigated by Faure-Beaulieu *et al.* (2021*a*): below a critical equivalence ratio, the thermoacoustic dynamics is characterized by noise-driven equiprobable intermittent transitions between CW and CCW mixed modes; when the equivalence ratio is slowly increased beyond this critical equivalence ratio, the mode chooses one spinning direction and no further direction reversal is observed; the inherent stochastic forcing from the turbulent combustion noise is then too weak to induce any further erratic transitions across the potential barrier of the underlying symmetric 'sombrero' potential. If several quasi-steady sweeps of equivalence ratio are performed through the threshold, CW and CCW spinning are equiprobable as final state, i.e. the state probability symmetry is recovered in the sense of ensemble average.

Spontaneous rotational symmetry breaking – corresponds to situations where a transition from a rotationally symmetric thermoacoustic dynamics (spinning mode or mixed mode whose standing component exhibits a drifting nodal line orientation) to symmetry-broken dynamics (mixed mode with standing component exhibiting a fixed nodal line orientation) occurs when a system parameter is quasi-steadily varied across a critical value, although the annular configuration is symmetric. So far, no experimental evidence of this type of symmetry breaking has been reported.

Bearing all this in mind, let us turn now to the phenomenon investigated in the present work: several studies based on nominally axisymmetric combustors have reported observations of preferred orientation of azimuthal modes (Worth & Dawson

2013; Bourgouin *et al.* 2015*a*; Faure-Beaulieu *et al.* 2021*a*; Kim *et al.* 2021). These observations are manifestations of explicit rotational symmetry breaking in spite of the fact that these combustors were designed to be rotationally symmetric, in contrast to the studies of Dawson & Worth (2013) and Aguilar *et al.* (2021) where the symmetry is deliberately broken by using baffles or different types of burners. In this work, we will explain this hitherto unexplained phenomenon, elucidating why imperceptible system asymmetries have a highly detectable effect on the thermoacoustic dynamics in the vicinity of the Hopf bifurcation. To that end, the change of phase space topology across the transition from linearly stable azimuthal thermoacoustic modes to limit cycles, both forced by turbulence-induced broadband internal noise, will be unravelled and modelled: we will show that the route to a self-sustained quasi-pure spinning mode passes through stationary states that are characterized by mixed modes whose standing component exhibits a statistically prevailing orientation and intermittent reversals of the spinning component direction. For the first time, we derive and solve numerically the Fokker–Planck equation corresponding to the model of Faure-Beaulieu & Noiray (2020). We show that this one-dimensional model fully reproduces the modal dynamics of the three-dimensional experimental annular combustor. Finally, we demonstrate that symmetrically designed combustors will always display explicit rotational symmetry breaking of the thermoacoustic modes at the bifurcation.

2. Experimental evidence of explicit and spontaneous symmetry breaking

Experiments were conducted using an annular combustor with 12 premixed flames operated at atmospheric conditions (see figure 1) and fuelled with a mixture of 70 % H_2 and 30 % CH_4 by power. The thermal power was fixed to 72 kW and the equivalence ratio was used as a bifurcation parameter. It was changed by adjusting the air mass flow, while keeping the fuel mass flow constant. It was varied between 0.4875 and 0.575 in steps of 1.25×10^{-2}. The collected dataset which is used here to investigate the unexpected explicit rotational symmetry breaking of the thermoacoustic dynamics, is the same as the one used by Faure-Beaulieu *et al.* (2021*a*) to investigate the spontaneous reflectional symmetry breaking. The hydrogen–methane–air mixture is fed into a cylindrical plenum located at the bottom part of the combustor in figure 1(*a*). This plenum conditions and divides the flow into 12 axisymmetric burners. The burners are composed of 150 mm long tubes of 18.9 mm diameter, with central rods terminated by bluff bodies of 13 mm diameter. Just downstream of these bluff bodies, hot products recirculate, which ensures robust anchoring of the flames. In contrast to experiments by Worth & Dawson (2013), the burner tubes are not equipped with a swirler, which is another typical element of gas turbine burners used to further strengthen the flame anchoring (Chterev *et al.* 2014). The burners are equally spaced around the circumference of the annular combustor, i.e. with 30° between each injector, as shown in the top view of the combustion chamber in figure 1(*c*). The inner and outer walls of the chamber were 120 and 300 mm long, respectively, with diameters of 127 and 212 mm. They were water cooled, enabling long run times and equilibrium wall temperatures.

Twelve Kulite (XCS-093-05D) pressure transducers were mounted at six azimuthal and two longitudinal positions flush with the inner wall of the burner tubes and recorded with a sampling rate of 51.2 kHz. The natural chemiluminescence of the flames viewed from the exhaust is recorded with a high speed camera using the same optical system as in the paper of Worth & Dawson (2013). Figure 2(*a*) shows the averaged chemiluminescence, which can be considered as proportional to the heat-release rate in

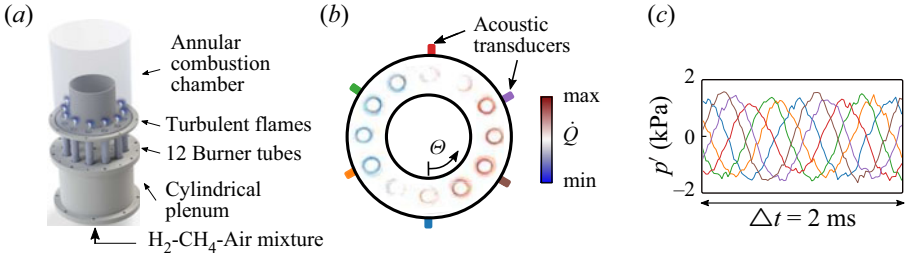

Figure 1. (*a*) Model gas turbine combustor. (*b*) Phase-averaged flame chemiluminescence. (*c*) Acoustic pressure recorded with six transducers. During the selected interval, the thermoacoustic limit cycle is a quasi-purely spinning eigenmode.

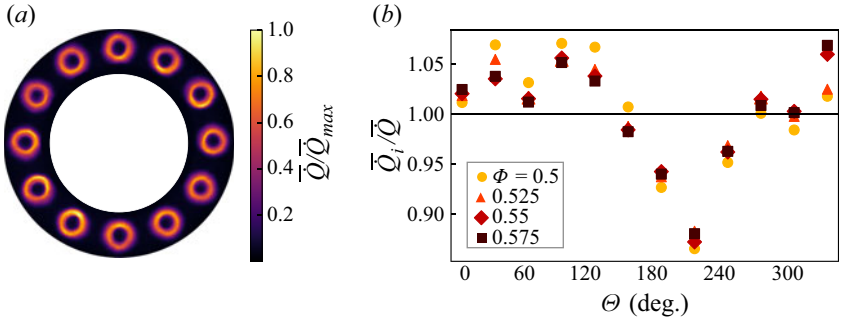

Figure 2. (*a*) Averaged overhead heat-release rate for $\Phi = 0.5$. (*b*) Heat release rate per burner normalized by the average heat-release rate.

this perfectly premixed configuration, for a thermoacoustically stable operating point at $\Phi = 0.5$. Figure 2(*b*) depicts the time-averaged heat-release rate per burner for several operating conditions, showing small discrepancies between the flames with a standard deviation of approximately 5 %, although the burners are designed to be identical and the cylindrical plenum to be axisymmetric. For each Φ, the combustor was ignited, run for at least 60 s to reach thermal equilibrium before recording 100 s of acoustic data while keeping the operating condition constant, and then turned off. The sound pressure level (SPL) in the annular combustor is plotted in figure 3(*a*) for four Φ. When $\Phi = 0.5$, the thermoacoustic system is linearly stable. The strongest resonance corresponds to an eigenmode whose azimuthal distribution exhibits one acoustic wavelength along the annular chamber circumference, and whose frequency is approximately 1090 Hz. The resonance oscillation of the different modes is sustained by the inherent broadband acoustic forcing from the turbulent combustion process. For larger Φ, the acoustic energy production resulting from the constructive thermoacoustic feedback exceeds the acoustic energy dissipation, and the dominant eigenmode becomes linearly unstable. Under these conditions, thermoacoustic limit cycles are reached at the aforementioned resonance frequency (Noiray & Schuermans 2013*a*). Their dynamics is governed by the nonlinear coherent response of the flame to the acoustic field and by the turbulent fluctuations of the heat-release rate.

Figure 3(*b*) presents the acoustic pressure p at three azimuthal locations during two short intervals (I) and (II) of the 100 s record for $\Phi = 0.55$, for which the self-sustained azimuthal thermoacoustic mode spins in the CCW and in the CW direction.

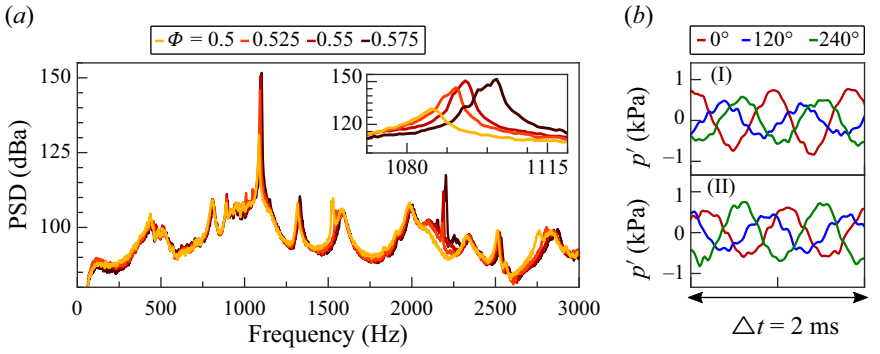

Figure 3. (*a*) SPL for increasing Φ. (*b*) Selected intervals for $\Phi = 0.55$, during which the azimuthal mode is mixed, with CW and CCW spinning directions. The angles in the legend correspond to the locations of the transducers.

Recently, Ghirardo & Bothien (2018) proposed a new ansatz for the acoustic pressure field based on quaternions to describe azimuthal eigenmodes in annular combustors. A set of four state variables A, θ, χ and φ, which vary slowly with respect to the fast acoustic time scale $2\pi/\omega$, and which can be extracted from the acoustic pressure time series, allows the following well-defined description of the state of an azimuthal thermoacoustic mode:

$$\tilde{p}(\Theta, t) = A(t)\, \mathrm{e}^{i(\theta(t)-\Theta)}\, \mathrm{e}^{-k\chi(t)}\, \mathrm{e}^{j(\omega t+\varphi(t))}, \tag{2.1}$$

where t and Θ are the time and the azimuthal coordinate, and i, j and k are the quaternion units. The acoustic pressure is $\mathrm{Re}(\tilde{p})$. It can be expanded as

$$p(\Theta, t) = A\cos(\Theta-\theta)\cos(\chi)\cos(\omega t+\varphi) + A\sin(\Theta-\theta)\sin(\chi)\sin(\omega t+\varphi), \tag{2.2}$$

and A is the real-valued positive slowly varying amplitude. The slowly varying angle θ describes the position of the anti-nodal line and the eigenmode state is identical for θ and $\theta+\pi$. The slowly varying angle χ indicates whether the azimuthal eigenmode is a standing wave ($\chi = 0$), a pure CW or CCW spinning wave ($\chi = \mp\pi/4$) or a mix of both for $0 < |\chi| < \pi/4$. The angle φ stands for slow temporal phase drift. These variables fully describe the acoustic fields p as a function of the time and azimuthal position.

Figure 4(*a*) shows the time traces of the extracted slow-flow variables together with their probability density functions (PDFs) for the last 6 s of the record, an interval that is representative of the stationary dynamics when $\Phi = 0.55$. The joint PDF of the first three state variables deduced from the 100 s record at $\Phi = 0.55$ is also shown in figure 5(*b*), where A, θ and 2χ are taken as spherical coordinates as shown in figure 5(*a*).

At the condition $\Phi = 0.55$, the amplitude of the azimuthal mode has a relatively small standard deviation compared with its mean value. The intermittent changes of sign of the nature angle χ correspond to changes of spinning direction of the mixed mode, as shown in figure 3(*b*). Although the difference is small, the most probable orientation of the anti-nodal line of the mixed mode's standing component is not the same whether the mode spins CW or CCW, a phenomenon that had never been reported and that will be explained at the end of the paper.

We now consider the evolution of the state variable PDFs in the vicinity of the Hopf bifurcation. These stationary PDFs are shown in the left column of figure 6 for several values of the bifurcation parameter Φ. Also, the time evolution of these state variables during 6 s intervals at four of the stationary operating conditions are presented in figure 7.

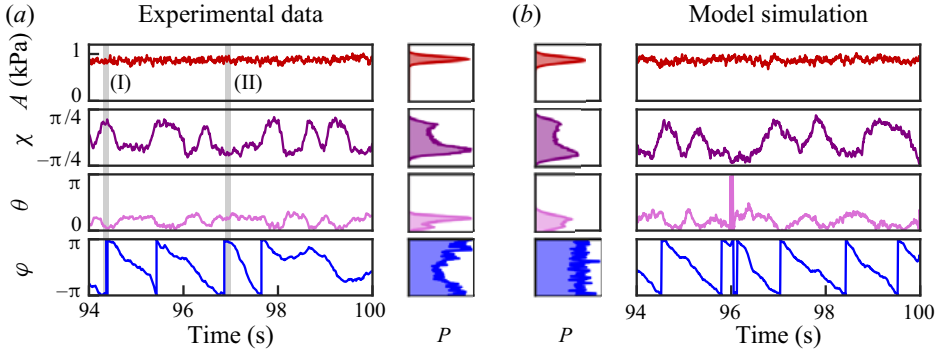

Figure 4. (*a*) Evolution of slow-flow variables that define the state of the azimuthal thermoacoustic mode, during the last 6 s of the experimental record for $\Phi = 0.55$, together with their PDFs. (*b*) PDFs and time traces from the time-domain simulations of (6.5), which includes both resistive and reactive asymmetries ($\varepsilon = 0.0023$, $\Theta_\varepsilon = 0.66$ rad, $\Gamma/\omega^2 = 4.2 \times 10^5$ Pa^2 s^{-1}, $\nu = 17$ s^{-1}, $c_2\beta = 17$ s^{-1}, $\Theta_\beta = 0.63$ rad and $\kappa = 1.2 \times 10^{-4}$ Pa^{-2} s^{-1}).

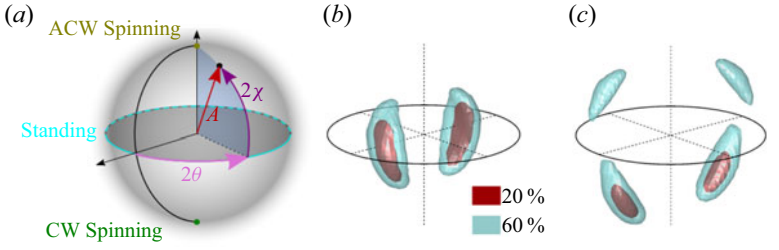

Figure 5. (*a*) Bloch sphere representation of the state of the azimuthal mode. (*b*,*c*) Experimental joint PDFs for $\Phi = 0.525, 0.55$.

The evolution of $P(A)$, shown in figure 6(*a*), is typical of a supercritical Hopf bifurcation in presence of additive random forcing (Juel, Darbyshire & Mullin 1997). The bifurcation occurs around $\Phi = 0.5125$. This point separates broadband-noise-driven resonances, when the azimuthal thermoacoustic mode is linearly stable, from limit cycles, when it is linearly unstable. The change of the mean amplitude is relatively smooth, which allows us to exclude the possibility of a sub-critical Hopf bifurcation, such as the ones investigated by Gopalakrishnan *et al.* (2016) or Noiray (2017). Next, one can consider how $P(\varphi)$ changes with Φ in figure 6(*d*). Overall, the slowly varying temporal phase φ drifts sufficiently during these 100 s records to yield rather flat distribution between 0 and 2π. One can notice that some phases are statistically prevailing for the higher range of investigated Φ, but these PDF maxima differ from case to case, and moreover, they wane when longer time traces are considered for computing the statistics, in agreement with the model which we propose in this article.

More interesting are the statistics of θ and χ, which are respectively associated with an explicit rotational symmetry breaking and with a spontaneous reflectional symmetry breaking of the thermoacoustic dynamics in this work. Let us begin with $P(\theta)$ in figure 6(*c*): even though the combustor was designed as rotationally symmetric as possible with a discrete rotational symmetry of order 12 (due to the 12 burners), the experimental results show a clearly preferred and repeatable anti-nodal line position for the different Φ. Given the long run times and the high-order discrete rotational symmetry of the chamber, one would either expect a quasi-uniform distribution of θ or a new preferred nodal line direction each time the combustor is ignited. The only explanation for the repeatable

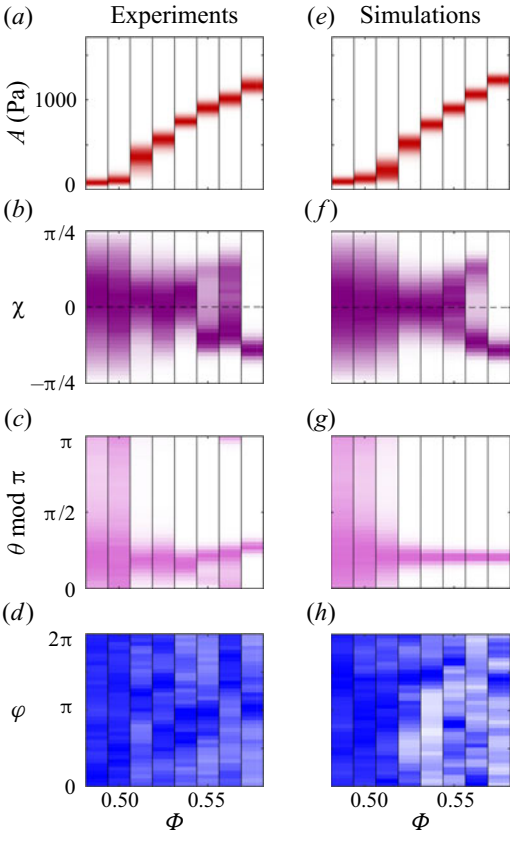

Figure 6. Stationary PDFs of A, χ, θ and φ at several Φ in the vicinity of the supercritical Hopf bifurcation. The PDFs are deduced from the slow-flow variable time traces, which are extracted from the acoustic pressure time traces following the procedure in Ghirardo & Bothien (2018). For (*a*)–(*d*), the acoustic time traces were obtained experimentally. For (*e–h*), the acoustic time traces were obtained by simulating 100 s of (3.1). Linear dependencies with respect to Φ of the parameters (ν, $c_2\beta$, κ, Γ) were deduced from the data processing and presented in figure 9. For the simulations, Θ_β has simply been kept at a constant value of 0.63 rad, which corresponds to the average value of θ observed in the experiments. The spontaneous reflectional symmetry breaking of the thermoacoustic dynamics, i.e. a clearly preferred spinning direction, is seen in the PDF of χ and occurs when Φ is increased from from 0.5625 to 0.575. The explicit rotational symmetry breaking of the thermoacoustic dynamics, i.e. a clearly preferred nodal line orientation, manifests itself in the PDF of θ and is visible for the entire range of Φ.

preferred orientation is the presence of an explicit rotational symmetry breaking in the thermoacoustic system.

In addition to this explicit rotational symmetry breaking, the thermoacoustic dynamics exhibits a spontaneous reflectional symmetry breaking, which has been investigated by Faure-Beaulieu *et al.* (2021*a*) and which manifests itself in figure 6(*b*): When $\Phi < 0.55$, $P(\chi)$ is unimodal, with a maximum close to zero, indicating that the thermoacoustic mode is mixed, with predominant standing wave component, which corroborates the theoretical studies from Faure-Beaulieu & Noiray (2020) and Ghirardo & Gant (2021). Considering figure 7, one can see that the underlying time traces exhibit erratic fluctuations of χ around 0. For $0.55 \leq \Phi \leq 0.5625$, $P(\chi)$ is bimodal, which indicates that the spinning wave component of the mixed mode is predominant. The intermittent changes of spinning direction for $\Phi = 0.55$, shown in figures 4(*a*) and 7, are less frequent and more pronounced

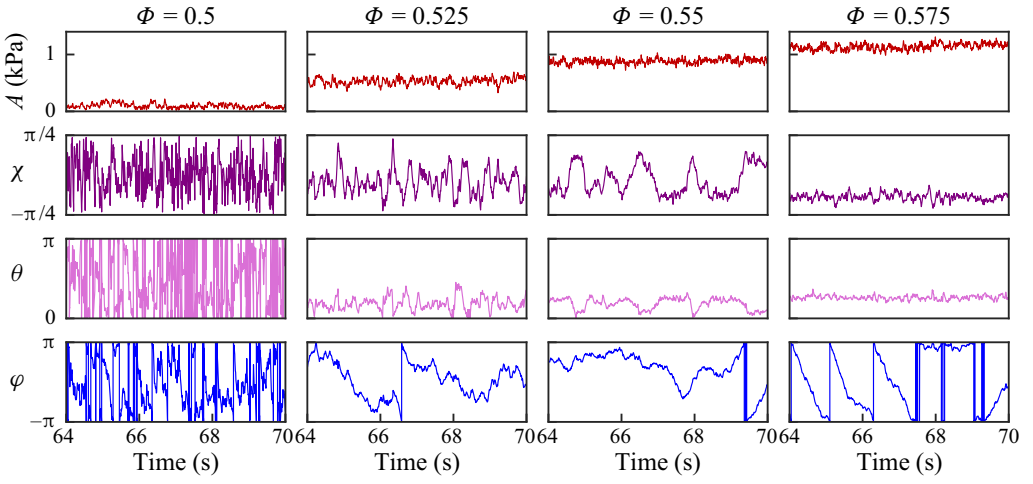

Figure 7. Experimental time traces of the state variables under stationary operating condition for different equivalence ratios. The duration of these time traces (6 s) is the same as the one presented in figure 2(*c*) of the main document. The extraction of the instantaneous state variables A, χ, θ and φ from the acoustic pressure signals is performed using the method proposed in Ghirardo & Bothien (2018).

than for $\Phi = 0.525$. When the equivalence ratio is further increased to $\Phi = 0.575$, one can see in figure 6(*b*) that the sporadic reversals of spinning direction do not take place anymore: the mixed mode spins in the CW direction and the symmetry of its state PDF is spontaneously broken beyond this threshold. As explained by Faure-Beaulieu *et al.* (2021*a*), this spontaneous reflectional symmetry breaking is due to the fact that the intensity of the inherent stochastic forcing is too low to induce further crossing of the potential barrier separating the CW and the CCW attractors. It is worth noting that, when the combustor is ignited and ramped up to $\Phi = 0.575$, the final stationary thermoacoustic state can also be the CCW mixed mode, which is shown in figure 8, and which demonstrates that both attractors coexist. The model presented in the remainder of this article, reproduces both the reflectional spontaneous symmetry breaking and the unexpected rotational explicit symmetry breaking.

3. Thermoacoustic wave equation

In the work of Faure-Beaulieu & Noiray (2020), the quaternion acoustic field was inserted into the following wave equation with distributed heat-release rate fluctuations to model the thermoacoustic dynamics of an idealized thin annular chamber:

$$\frac{\partial^2 p}{\partial t^2} + \alpha \frac{\partial p}{\partial t} - \frac{c^2}{\mathcal{R}^2} \frac{\partial^2 p}{\partial \Theta^2} = (\gamma - 1)\, \frac{\partial \dot{Q}}{\partial t} + \Xi(\Theta, t). \tag{3.1}$$

In this equation, α is the acoustic damping at the annulus boundaries, $\mathcal{R}$ the annulus radius, c the speed of sound, γ the heat capacity ratio, $\dot{Q}(\Theta, t)$ the coherent component of the heat-release-rate fluctuations and Ξ a spatially distributed white Gaussian noise representing the effect of turbulent fluctuations of the heat-release rate (e.g. Clavin, Kim & Williams 1994; Lieuwen 2003; Lieuwen & Banaszuk 2005; Noiray & Schuermans 2013*a*). The coherent heat-release-rate fluctuations are then linked to the acoustic field using the

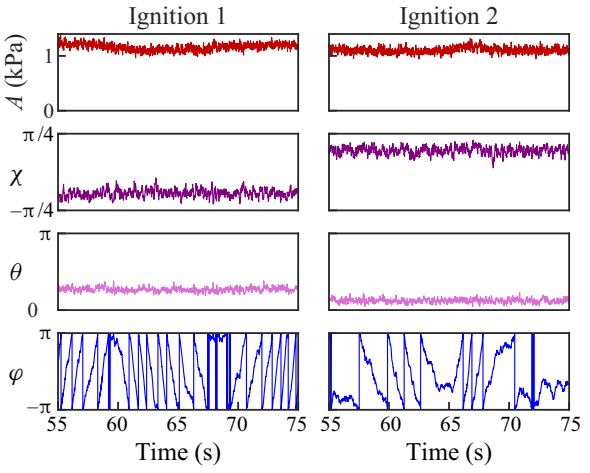

Figure 8. Experimental time traces of the state variables at $\Phi = 0.575$ a thermal power of 72 kW. Two independent tests were performed. For each of them, the annular combustor is ignited and set to the same operating condition $\Phi = 0.575$. The twenty seconds time traces of χ show that the final steady state can either be a CW mixed mode or a CCW one.

expression

$$(\gamma - 1)\dot{Q} = \beta[1 + c_2 \cos(2(\Theta - \Theta_\beta)]p - \kappa p^3. \tag{3.2}$$

The first term stands for the linear response of the fluctuating heat-release rate to acoustic perturbations. If $\beta > \alpha$ and $c_2 = 0$, the linear growth rate of the thermoacoustic mode $\nu = (\beta - \alpha)/2$ is positive, i.e. the mode is linearly unstable, and small acoustic perturbations are exponentially amplified. This pure exponential growth is not observed in real combustors because of the inherent turbulence-induced stochastic forcing Ξ and because of the nonlinearity of the flame response to the acoustic field beyond a certain level. The first term also accounts for spatial non-uniformities along the annulus, through the second component $c_2 \cos(2(\Theta - \Theta_\beta))$ of the Fourier series of any distribution of heat-release-rate source, which is the only component influencing the first azimuthal eigenmode as shown by Noiray *et al.* (2011). Given that real nominally symmetric combustors always exhibit some small asymmetries – this fact is exemplified by the mean heat-release-rate distribution of the present experimental system shown in figure 2 – it is crucial to use this Fourier series in the model, because it will be shown that even imperceptible non-uniformities of the thermoacoustic coupling have a significant observable effect close to the bifurcation. The angle Θ_β is the direction of maximum root mean square acoustic pressure. In the theoretical studies of Noiray *et al.* (2011) and Faure-Beaulieu & Noiray (2020), the assumption $\Theta_\beta = 0$ was made for simplicity, and without loss of generality, because the origin of Θ can be chosen arbitrarily. In the present work, we keep the same origin for all the operating points because the preferential orientation of the mode can vary for different operating conditions. The second term of (3.2), $-\kappa p^3$, defines the saturation of flame response, which leads to limit cycle oscillations, and is sufficient to adequately capture the thermoacoustic dynamics in the vicinity of supercritical Hopf bifurcations as in the works from Lieuwen (2003), Noiray & Denisov (2017), Hummel *et al.* (2018) and Lee *et al.* (2021). Possible non-uniformities of the nonlinear term are not accounted for in order to ease the parameter identification process. The modelling assumptions are now discussed in more detail.

First, real annular combustors have an overall toroidal shape but they also include complex three-dimensional (3-D) geometrical features. Consequently, their acoustic field can only be predicted using the 3-D wave equation. However, in the present paper, we are only interested by the azimuthal distribution of the acoustic modes at fixed radial and axial positions. Therefore, we can describe the dynamics of this azimuthal component with a one-dimensional (1-D) wave equation (e.g. Noiray & Schuermans 2013*b*; Faure-Beaulieu & Noiray 2020; Faure-Beaulieu *et al.* 2021*b*).

Then, the saturation of the flame response to acoustic perturbations is simply modelled as $\dot{Q} = \beta p - \kappa p^3$, or $\dot{Q} = \beta p(1 + c_2 \cos(2(\Theta - \Theta_\beta))) - \kappa p^3$ in presence of second-order asymmetry in the linear thermoacoustic coupling term. This low-order model, with linear and cubic term only, is a valid description in the vicinity of a supercritical Hopf bifurcation. Higher-order polynomials or sigmoid-type functions could be used to extend its validity further away from the Hopf point (Noiray 2017; Bonciolini *et al.* 2021; Lee *et al.* 2021). However, using a more elaborate nonlinear flame response model complicates the parameter identification. Considering that in this article, we focus on the neighbourhood of the Hopf point, we use the simple cubic nonlinearity, which corresponds to the normal form of the bifurcation.

Furthermore, considering that, in practice, coherent heat-release-rate oscillations resulting from acoustic perturbations occur after a certain convective delay, it may seem inappropriate to omit this phase lag in the model for $\dot{Q}$. Indeed, acoustic pressure fluctuations in the combustion chamber and in the plenum induce coherent velocity and equivalence ratio perturbations in the burners which do not instantaneously propagate to the flame, i.e. there is a phase lag between the acoustic field and the coherent heat-release-rate response. A model with such phase lag was derived by Faure-Beaulieu & Noiray (2020) but it is not used in this paper for the following reasons: firstly, accounting for a convective delay in this model does not substantially change the phase space topology when it is short compared with the inverse of the thermoacoustic growth rates, which is usually true in practice. The interested reader can refer to the work by Bonciolini *et al.* (2021) where the validity of this simplification for low-order modelling of thermoacoustic instabilities is discussed in detail. Secondly, accounting for it would necessitate the identification of an additional parameter (the time delay), which cannot be achieved in a robust manner with the observables (acoustic pressure signals at six azimuthal locations in the annular combustor) considered in the present work.

Next, it is worth mentioning that a nonlinear flame response model, which depends not only on the acoustic pressure load across the burners but also on the azimuthal acoustic velocity in the annular chamber, has also been proposed by Ghirardo & Juniper (2013). In that paper, a deterministic analysis shows that, with such a flame response model, standing modes can be attractors even in the absence of asymmetry. In that scenario, the nodal line direction is solely defined by the initial condition. This means that, in practice, it would stabilize at a random value after each ignition of the combustor. It would thus not exhibit a statistically prevailing direction, which is indisputably an evidence of spatial asymmetry in the configuration, and which we observe in the present work. The theoretical work of Ghirardo & Juniper (2013) followed, and inspired experimental and theoretical studies (e.g. O'Connor & Lieuwen 2011; Acharya *et al.* 2014; Saurabh & Paschereit 2017; Smith *et al.* 2018; Li *et al.* 2019) where combinations of axial and transverse acoustic forcing of compact swirled turbulent flames were considered. Besides, it can be noted that, in the work of Berger *et al.* (2017) and of Hummel *et al.* (2017), the response of a non-compact swirled flame to transverse acoustic excitation was investigated for the case of high frequency thermoacoustic instabilities. However, since a simple model, which only

involves the acoustic pressure load across the burners, allows us to satisfactorily reproduce and explain the main experimental observations, we do not include the additional possible effect of the azimuthal acoustic velocity in our flame response model.

Another relevant mechanism that is not considered in our model is the effect of the mean azimuthal flow on the thermoacoustic coupling, which was recently investigated by Bauerheim, Cazalens & Poinsot (2015) and Faure-Beaulieu & Noiray (2020). Indeed, it is predicted in § IX of Faure-Beaulieu & Noiray (2020) that, for an idealized combustor with heat-release rate occurring in a region with a net azimuthal flow, the spinning mode rotating against the azimuthal mean flow direction attracts the dynamical system with more strength than the co-rotating spinning mode. This mechanism could be a possible explanation for very recent experimental observations by Ghirardo *et al.* (2021). In the latter work, the authors used a combustor with the same architecture and main dimensions as in the present paper. However, they had more burner tubes (18 instead of 12) and these burners were equipped with axial swirlers. Consequently, the reactive flow field in the combustor substantially differed from the one studied in this work. In particular, one can see in figure 2 of Ghirardo *et al.* (2021), that the mean heat-release rate is concentrated toward the inner radius of the annular combustion chamber, where the co-rotating swirling flames, uniformly distributed along the annulus, impart a CW swirling motion to the flow. On the other hand, towards the outer radius, there is a bulk swirling motion in the CCW direction, as it was sketched with black arrows in figure 1(*c*) of Worth & Dawson (2014). Assuming that the coherent fluctuating heat-release rate is more intense toward the inner wall of the chamber, where the mean heat-release rate is larger and where the flow exhibits a substantial bulk azimuthal velocity in the CW direction, the theory proposed in § IX of Faure-Beaulieu & Noiray (2020) could be an explanation for the reported predominance of the CCW spinning thermoacoustic mode with this particular combustor. One can also note that these observations are in agreement with the forced experiments reported by Nygård *et al.* (2019). Now, considering that in the present work, the burner tubes do not have swirlers, it can be assumed that the hot product velocity in the annulus does not exhibit an azimuthal component. Therefore, this feature of the model from Faure-Beaulieu & Noiray (2020) is not included in this work.

The parameters of the model given by (3.1) and (3.2) can be identified from the experimental data. To that end, we do not use the acoustic pressure time traces directly. Instead, we consider the time evolution of the state variables A, θ, χ and φ, which can be extracted from the acoustic pressure traces, in order to achieve a robust model-based and data-driven parameter identification. In fact, this method necessitates a time-domain model for the state variables, which is presented in § 4. Once identified, the parameters will be used to perform time-domain simulations of (3.1) in § 5.

4. Langevin equation for the state variables

The coupled Langevin equations for A, θ, χ and φ, derived by Faure-Beaulieu & Noiray (2020) by performing spatial and temporal averaging of (3.1), are very convenient to perform parameter identification, because they allow us to separate the contribution of the different parameters in distinct equations and therefore to reliably identify them. This system of equation is written as

$$\dot{\boldsymbol{Y}} = \boldsymbol{F}(\boldsymbol{Y}) + \boldsymbol{B}(\boldsymbol{Y})\boldsymbol{N}, \tag{4.1}$$

and governs the dynamics of the azimuthal mode state vector $\boldsymbol{Y} = (A, \chi, \theta, \varphi)^T$ via a deterministic contribution $\boldsymbol{F}(\boldsymbol{Y})$ and a stochastic forcing term $\boldsymbol{B}(\boldsymbol{Y})\boldsymbol{N}$, where

$\boldsymbol{N} = (\zeta_A, \zeta_\chi, \zeta_\theta, \zeta_\varphi)^T$ is a vector of independent white Gaussian noises of intensity $\Gamma/2\omega^2$. The latter intensity involves the constant Γ, which is the spatially averaged stochastic forcing level originating from the turbulent fluctuations of the heat-release rate. The expressions for $\boldsymbol{F}$ and $\boldsymbol{B}$ were derived by Faure-Beaulieu & Noiray (2020) and are given below

$$F_A(\boldsymbol{Y}) = \left(\nu + \frac{c_2\beta}{4}\cos(2(\theta - \Theta_\beta))\cos(2\chi)\right)A - \frac{3\kappa}{64}(5 + \cos(4\chi))A^3 + \frac{3\Gamma}{4\omega^2 A}, \tag{4.2}$$

$$F_\chi(\boldsymbol{Y}) = \frac{3\kappa}{64}A^2\sin(4\chi) - \frac{c_2\beta}{4}\cos(2(\theta - \Theta_\beta))\sin(2\chi) - \frac{\Gamma\tan(2\chi)}{2\omega^2 A^2}, \tag{4.3}$$

$$F_\theta(\boldsymbol{Y}) = -\frac{c_2\beta}{4}\frac{\sin(2(\theta - \Theta_\beta))}{\cos(2\chi)}, \tag{4.4}$$

$$F_\varphi(\boldsymbol{Y}) = \frac{c_2\beta}{4}\sin(2(\theta - \Theta_\beta))\tan(2\chi), \tag{4.5}$$

where we introduced $\nu = (\beta - \alpha)/2$, which is the linear growth rate of the amplitude A in absence of asymmetries ($c_2 = 0$), and where

$$\boldsymbol{B}(\boldsymbol{Y}) = \begin{pmatrix} 1 & 0 & 0 & 0 \\ 0 & A^{-1} & 0 & 0 \\ 0 & 0 & (A\cos(2\chi))^{-1} & 0 \\ 0 & 0 & -\tan(2\chi)/A & A^{-1} \end{pmatrix}. \tag{4.6}$$

The analysis of the equilibrium points of $\dot{\boldsymbol{Y}} = \boldsymbol{F}(\boldsymbol{Y})$ was performed in Faure-Beaulieu & Noiray (2020), where it was shown that, for an ideal axisymmetric geometry with $c_2 = 0$ and $\Gamma \neq 0$, the attractor of the deterministic part of (4.1) is a mixed mode when $27\kappa\Gamma/(256\nu^2\omega^2) < 1$ or otherwise a standing mode. In both cases, the instantaneous anti-nodal line θ drifts slowly according to a random walk. For annular chambers featuring a certain degree of azimuthal asymmetry but without stochastic forcing ($c_2 \neq 0$ and $\Gamma = 0$), the attractors are mixed modes if $c_2\beta/(2\nu) < 1$ and otherwise standing modes, which was already found in Noiray *et al.* (2011).

This model cannot be used to predict the stability and slow-flow dynamics of a real combustor from the knowledge of its geometry and operating condition. However, as mentioned above, we show here that its handful of parameters $[\nu; c_2\beta; \kappa; \Gamma]$ can be identified from the experimental data and then the model can reproduce the thermoacoustic dynamics.

Several methods are available for disentangling deterministic and stochastic contributions in stochastic trajectories (e.g. Brückner, Ronceray & Broedersz 2020; Ferretti *et al.* 2020; Frishman & Ronceray 2020). Here, we use a method, which was adapted from the work of Friedrich and co-workers (Siegert, Friedrich & Peinke 1998; Friedrich *et al.* 2002; Böttcher *et al.* 2006; Friedrich *et al.* 2011) to the investigation of nonlinear oscillators subject to random forcing (e.g. Noiray & Schuermans 2013*a*; Bonciolini, Boujo & Noiray 2017; Boujo & Noiray 2017; Noiray & Denisov 2017; Boujo *et al.* 2020), and which was applied to thermoacoustic and aeroacoustic instabilities. More recently, this framework was further developed and used for the analysis of global hydrodynamic instabilities in turbulent flows (e.g. Lee *et al.* 2019; Callaham *et al.* 2021; Sieber, Paschereit & Oberleithner 2021).

First, for each Φ, the transition probabilities of the state variables are extracted. Then, these probabilities are used to compute the first and second Kramers–Moyal coefficients

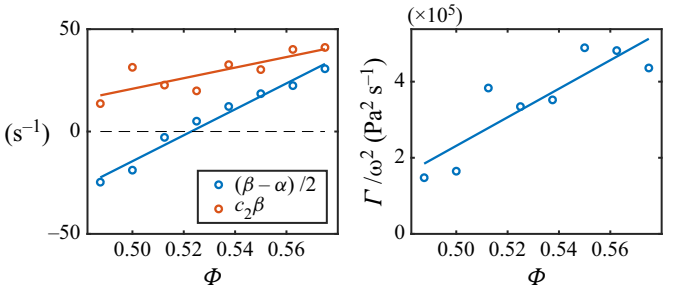

Figure 9. Parameters identified with the model-based data-driven approach explained in the Appendix A. The identified value for κ is 1.2×10^{-4} Pa^{-2} s^{-1}. Continuous lines show the linear regressions of the model parameters as a function of Φ.

that serve as basis for parameter identification with least square fitting. More details about the robustness of the parameter identification are given in the Appendix A of this article. The results of this model-based data-driven parameter identification are presented in figure 9. It was found that simple linear regression for the dependencies of $\nu = (\beta - \alpha)/2$, $c_2\beta$, κ and Γ on Φ allows to unravel the complex topology of the phase space. Indeed, in § 5, these parameters are used to run time-domain simulations of the wave equation (3.1) to generate 100 s acoustic time series for each Φ, from which the state variables and their statistics are extracted and successfully compared with the ones of the experiments.

5. Time-domain simulations of the thermoacoustic dynamics

For each of the values of Φ considered in the experiments, a time-domain simulation of the thermoacoustic problem given by (3.1) and (3.2) is performed with the identified linear functions of Φ for the model parameters ν, $c_2\beta$ and Γ/ω^2 that are shown in figure 9. The numerical approach for these simulations is explained below.

The geometry is 2π-periodic and the acoustic pressure field can be projected on the orthogonal basis formed by the eigenmodes of the homogeneous 1-D wave equation

$$p(t, \Theta) = \sum_{n=1}^{\infty} \eta_{a,n}(t)\cos(n\Theta) + \eta_{b,n}(t)\sin(n\Theta). \tag{5.1}$$

In the present case, the thermoacoustic instability is governed by a single eigenmode, whose azimuthal distribution corresponds to one acoustic wavelength. Therefore, only the first term of this expansion is kept and we use the ansatz $p(t, \Theta) = \eta_a(t)\cos(\Theta) + \eta_b(t)\sin(\Theta)$ in (3.1). As in Noiray & Schuermans (2013*b*), we project (3.1) on the orthogonal natural eigenfunctions $\cos(\Theta)$ and $\sin(\Theta)$ in order to obtain coupled oscillator equations for the standing components η_a and η_b

$$\left.\begin{aligned}
\ddot{\eta}_a + \omega^2\eta_a &= \left(2\nu + \frac{c_2\beta}{2}\cos(2\Theta_\beta) - \frac{\kappa}{4}(9\eta_a^2 + 3\eta_b^2)\right)\dot{\eta}_a \\
&\quad + \frac{c_2\beta}{2}\sin(2\Theta_\beta)\dot{\eta}_b - \frac{3}{2}\kappa\eta_b\eta_a\dot{\eta}_b + \zeta_a, \\
\ddot{\eta}_b + \omega^2\eta_b &= \left(2\nu - \frac{c_2\beta}{2}\cos(2\Theta_\beta) - \frac{\kappa}{4}(9\eta_b^2 + 3\eta_a^2)\right)\dot{\eta}_b \\
&\quad + \frac{c_2\beta}{2}\sin(2\Theta_\beta)\dot{\eta}_a - \frac{3}{2}\kappa\eta_a\eta_b\dot{\eta}_a + \zeta_b,
\end{aligned}\right\} \tag{5.2}$$

where $\omega = c/\mathcal{R}$ is the eigenfrequency of the first azimuthal mode, and ζ_a and ζ_b are independent Gaussian white noises of intensity Γ resulting from the projection of the turbulence-induced stochastic forcing $\Xi(\Theta, t)$ onto $\cos(\Theta)$ and $\sin(\Theta)$.

It should be noted that, in this section, we are not using the ansatz (2.2), which was considered for deriving the Langevin equations for the state variables. This is because, here, we want to resolve the fast acoustic dynamics with the identified model parameters, and the modal projection is just a convenient alternative to the direct simulation of the partial differential equation (3.1), where the only simplifying assumption is the truncation of the expansion to a single azimuthal mode.

Stochastic Runge–Kutta methods exist to solve stochastic differential equations with a white noise term, but unlike classic Runge–Kutta methods, their implementation becomes very complex when the discretization order is greater than 1. As the classical first-order stochastic methods need an excessively small time discretization to solve the second-order system (5.2), we adopt another method: ζ_a and ζ_b are first computed as independent Ornstein–Uhlenbeck processes, whose correlation time τ_c is very small compared with the acoustic period. The corresponding stochastic differential equation is $\tau_c \,\mathrm{d}\zeta = -\zeta \,\mathrm{d}t + \sqrt{\Gamma}\,\mathrm{d}W$, where $\mathrm{d}W$ is a Wiener process and Γ the noise intensity. It is readily solved with a first-order Euler–Maruyama scheme. Then, ζ_a and ζ_b are used as external forcing in (5.2), which are treated as ordinary differential equations that are integrated with a time step Δt that is small compared with the autocorrelation times of the dynamic noises. We set $\tau_c = 50$ µs and $\Delta t = 5$ µs. The acoustic period is $T \simeq 0.92$ ms, so $\tau_c/T \approx 5 \times 10^{-2}$, and ζ_a and ζ_b have the same effect on the modal dynamics as white noises of intensity Γ. It is important to stress that the additive stochastic forcing produced by the turbulent component of the heat-release-rate fluctuations is not a white noise, but its broadband nature usually allows us to safely approximate it as such (Bonciolini *et al.* 2017). The intensity Γ should thus be interpreted as the forcing level in a narrow frequency range around the thermoacoustic instability frequency of an effective white noise.

The model parameters, which have been identified by using the model-based data-driven method presented in the Appendix A, and which are shown in figure 9, are now used in (5.2) to perform time-domain simulations at each of the equivalence ratios considered in this work. The time traces of η_a and η_b are then used to reconstruct the spatio-temporal dynamics of the acoustic pressure in the annulus according to the ansatz $p(t, \Theta) = \eta_a(t)\cos(\Theta) + \eta_b(t)\sin(\Theta)$. From these simulated acoustic pressure data, the state variables are extracted and the results for four of the considered Φ are presented in figure 10. The time traces of the state variables in this figure are in close agreement with the ones extracted from the experimental data and shown figure 7. Their PDFs are then computed from 100 s simulations in order to also compare them with the experimental PDFs. The results are presented in figures 6(*e*)–6(*h*). The excellent match between the experimental PDFs and the ones from the simulations shows that, despite the simplifications invoked to derive the low-order model, it can quantitatively reproduce the dynamics of the state variables. In particular, both the explicit and the spontaneous symmetry breaking described in § 2 are reproduced by the model simulations.

6. Phase space topology

Now that the thermoacoustic wave equation model given by (3.1) and (3.2) has been validated against the present experimental observations, we use the corresponding Langevin equation (4.1) for the state variables to draw general conclusions about the

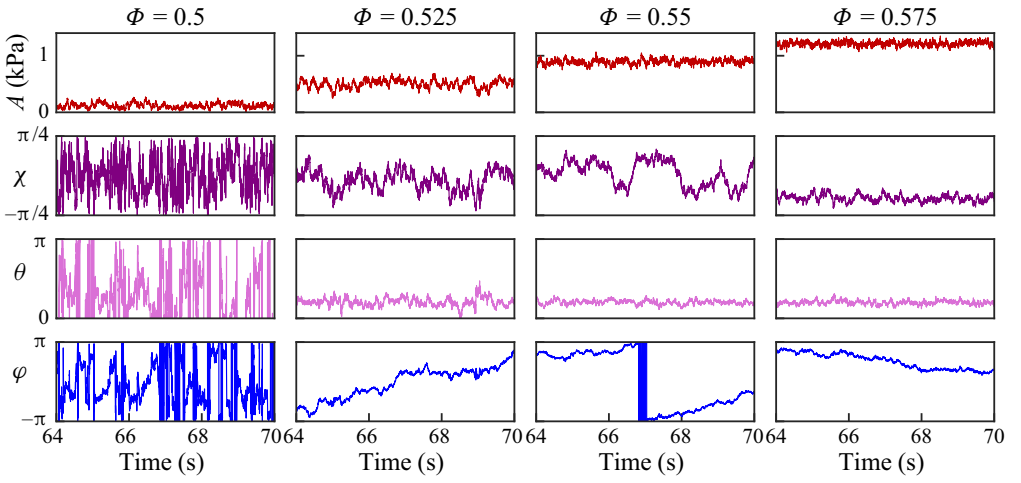

Figure 10. Time traces of the state variables A, χ, θ and φ, which were extracted from the simulated acoustic pressure field. The extraction of these instantaneous state variables is performed using the method proposed in Ghirardo & Bothien (2018).

thermoacoustic dynamics of azimuthal modes close to the Hopf bifurcation in real annular combustors.

The two coupled equations for A and χ recently allowed us to identify the fundamental mechanisms involved in the spontaneous symmetry breaking of the thermoacoustic mode state (Faure-Beaulieu *et al.* 2021*a*). In fact, the symmetry of the phase space is not broken, but beyond a certain linear growth rate, the symmetry of the state may be, if the mode chooses either the CW or the CCW spinning state and the noise is not sufficiently large to allow sporadic escape from and return to this attractor (Faure-Beaulieu *et al.* 2021*a*).

Here, we go significantly further by considering the stationary solutions of the Fokker–Planck equation governing the joint PDF of the state vector in order to provide a complete picture of the phase space topology. We will represent the PDF of the state vector with a Bloch sphere representation, and therefore exclude from the analysis the state variable φ, which is straightforward because it does not appear in the Langevin equations of the other state variables. We thus consider the first three components of the (4.1), which are written in compact form as

$$\dot{\boldsymbol{Z}} = \boldsymbol{G}(\boldsymbol{Z}) + \boldsymbol{C}(\boldsymbol{Z})\boldsymbol{M}(t), \tag{6.1}$$

where $\boldsymbol{Z} = (A, \chi, \theta)^T$, $\boldsymbol{G} = (F_A, F_\chi, F_\theta)^T$, $\boldsymbol{M} = (\zeta_A, \zeta_\chi, \zeta_\theta, \zeta_\varphi)^T$ and $\boldsymbol{C}$ is the submatrix of $\boldsymbol{B}$ composed of its first three lines. The Fokker–Planck equation (FPE) describing the time evolution of the PDF of the state vector $\boldsymbol{Z}$ is

$$\frac{\partial P(\boldsymbol{Z})}{\partial t} = -\frac{\partial G_i(\boldsymbol{Z})P(\boldsymbol{Z})}{\partial Z_i} + \frac{\partial^2 D_{ij}(\boldsymbol{Z})P(\boldsymbol{Z})}{\partial Z_i \partial Z_j}, \tag{6.2}$$

where the diffusion matrix $\boldsymbol{D} = (\Gamma/4\omega^2)\boldsymbol{C}\boldsymbol{C}^T$ is

$$\boldsymbol{D} = \frac{\Gamma}{4\omega^2}\begin{pmatrix} 1 & 0 & 0 \\ 0 & A^{-2} & 0 \\ 0 & 0 & \dfrac{1}{(A\cos(2\chi))^2} \end{pmatrix}. \tag{6.3}$$

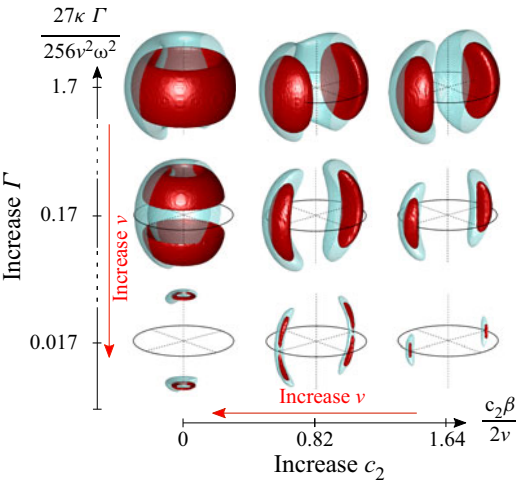

Figure 11. Stationary PDF of the eigenmode state computed with the FPE for different levels of noise intensity Γ and purely resistive asymmetry c_2 (state probability: 20 % and 60 %). The reference case in the centre of the bottom row corresponds to the parameters of the calibrated model for $\Phi = 0.55$.

There are only terms on the diagonal, and D_{AA} does not depend on A, $D_{\chi\chi}$ does not depend on χ and $D_{\theta\theta}$ does not depend on θ. The FPE then becomes

$$\frac{\partial P(\boldsymbol{Z})}{\partial t} = -\frac{\partial G_i(\boldsymbol{Z})P(\boldsymbol{Z})}{\partial Z_i} + D_{ii}(\boldsymbol{Z})\frac{\partial^2 P(\boldsymbol{Z})}{\partial^2 Z_i}. \tag{6.4}$$

The 3-D FPE (6.4) is solved in time, with an implicit time scheme, and symmetric 2-point stencils for the first-order derivatives with respect to the state variables (and symmetric 3-point stencils for the second-order derivatives). The problem is initialized with 3-D Gaussian distributions around the equilibrium values $(A, \chi, \theta) = (A_0, \chi_0, \theta_0)$ predicted by the deterministic part of the model for the given set of parameters, which accelerates the convergence of the simulation to the stationary PDF. Given that the angles θ and $\theta + \pi$ represent the same state, the problem is accordingly initialized with a superposition of two sets of Gaussian distributions. Absorbing boundary conditions are defined at $A = 0.1A_0$ and $A = 2A_0$, and at $\chi = \pm 0.9999\pi/4$ – and not in $\pm\pi/4$ because of the singularity of $\tan(2\chi)$. The probability leakage from these absorbing conditions is negligible because of the steep slope of $\tan(2\chi)$ around $\pm\pi/4$, which pushes the PDF away from these boundaries.

The case $\Phi = 0.55$ is taken as reference. The corresponding identified parameters are used in the 3-D FPE (6.4) to compute the stationary PDF, which is presented in the middle of the bottom row of figure 11. From this reference state vector PDF, we arbitrarily change the linear growth rate ν and the level of asymmetry c_2 for fixed κ and Γ. The resulting stationary solutions are presented around the reference PDF in figure 11.

Recalling that the eigenmode state is identical for θ and $\theta + \pi$, we start the description of this figure in the bottom right corner, where the state exhibits a unimodal PDF corresponding to a statistically prevailing standing mode with fixed anti-nodal line orientation. When the rotational asymmetry level is decreased, the PDF first becomes bimodal, which corresponds to a predominant mixed mode with intermittent changes of spinning direction. Ultimately, for $c_2 = 0$, the nodal line cannot lock anymore on a fixed orientation, it slowly drifts as a random walk and the PDF takes the form of two

tori close to the poles. These results are in line with previous findings from Noiray & Schuermans (2013*b*), which, however, only provided a simplified description of the phase space topology.

Then, the effect of noise and of the linear growth rate can be analysed by moving vertically in the diagram. For an ideal rotationally symmetric combustor (first column) and for a fixed turbulent forcing level Γ and saturation constant κ, the effect of decreasing the linear growth rate is seen by moving up: the two tori merge when the system is brought close enough to the Hopf point (top row), which means that the system undergoes a transition from predominantly spinning states to prevailing standing modes with single torus PDF. However, a key consequence of the model, which had not been drawn so far, is that this toroidal PDF will not be observed in real combustors, because the more the source term gain β tends to α, and thus $\nu = (\beta - \alpha)/2 \to 0$, the more $c_2\beta/(\beta - \alpha)$ will rise, which means that such decrease of β would be accompanied with a move towards the right on the diagram. In other words, the effect of a resistive asymmetry, however minute, will be magnified in the vicinity of the bifurcation, resulting in mixed modes with repeatable preferred orientation.

Finally, we can add to the model tiny reactive asymmetries, which also exist in any nominally symmetric real combustors due to inherent geometrical imperfections. They can alternatively result from a non-uniform temperature distribution (Noiray *et al.* 2011), or from a non-uniform reactive component of the flame and flow responses to acoustic perturbations as recently shown by Faure-Beaulieu *et al.* (2021*b*). Here, we include them in order to explain the small deviations between the model with purely resistive asymmetry and some of the experimental observations. Indeed, when $\Phi = 0.55$, there are small changes of the anti-nodal line angle θ, which are correlated with the change of spinning direction, and these changes are not retrieved from the model with purely resistive asymmetries. As in the work of Faure-Beaulieu *et al.* (2021*b*) – modelling of beating modes observed with the same combustor operated at significantly lower thermal power (48 kW) – we introduce an azimuthal modulation of the term $c^2/\mathcal{R}^2$ in the wave equation (3.1), which becomes

$$\frac{\partial^2 p}{\partial t^2} + \alpha\frac{\partial p}{\partial t} - (1 + \varepsilon\cos[2(\Theta - \Theta_\varepsilon)])\frac{c^2}{\mathcal{R}^2}\frac{\partial^2 p}{\partial \Theta^2} = (\gamma - 1)\frac{\partial \dot{Q}}{\partial t} + \Xi(\Theta, t), \qquad (6.5)$$

with the heat-release-rate response $\dot{Q}$ given by (3.2). In this equation, ε is the amplitude of the reactive asymmetry and Θ_ε its orientation: they correspond to parameters m_2 and $\Theta_{\mu 2}$ in the paper of Faure-Beaulieu *et al.* (2021*b*). After manual calibration of these two additional parameters by using the experimental data at $\Phi = 0.55$, which yields $\varepsilon = 0.0023$, $\Theta_\varepsilon = 0.03 + \Theta_\beta$, we can reproduce the jumps of θ and the asymmetry of the marginal PDF of χ. This is shown in figure 4(*b*), in which the slow-flow variables extracted from time-domain simulations of (6.5) are presented. As explained by Faure-Beaulieu *et al.* (2021*b*), the misalignment between the orientation Θ_β of the resistive asymmetries and the orientation Θ_ε of the reactive asymmetries breaks the reflection symmetry of the configuration which causes a preference for one of the two spinning directions. It is worth emphasizing that this tiny reactive asymmetry ($\varepsilon = 0.0023$) induces both the predominance of CW spinning modes and the small changes of θ synchronized with the changes of χ previously reported in figure 4.

7. Conclusions

In this paper, the thermoacoustic dynamics of an azimuthal mode in an annular combustor has been investigated experimentally and theoretically. Previous studies on this topic

focused on isolated operating conditions, and one of the novelties of the present work is that we reveal the complexity of the phase space for a range of conditions around the bifurcation that separates linearly stable thermoacoustic states from limit cycles. We show that our model closely reproduces the experimentally observed spontaneous and explicit symmetry breaking of the azimuthal mode dynamics. Accounting for the presence of both resistive and reactive asymmetries, this model allows us to explain the predominance of a spinning direction, as well as the changes of preferred nodal line orientation, which are synchronized with the intermittent changes of spinning direction.

The occurrence of the explicit rotational symmetry breaking, in the form of a statistically dominant direction for the nodal line of the standing component of the eigenmode, was not expected because the present combustor has been designed to be nominally symmetric. We explain this surprising phenomenon with our model, by demonstrating that there is a magnifying lens effect of tiny asymmetries at the bifurcation. This key finding results from the fact that real annular chambers are always imperfect, and that these imperfections, no matter how small, will be highly visible at the bifurcation and strongly influence the stochastic modal dynamics. We can thus conclude that manufacturing annular combustors free from explicit rotational symmetry breaking at the bifurcation is out of reach.

Declaration of interests. The authors report no conflict of interest.

Funding. This project has received funding from the European Union's Horizon 2020 Research and Innovation Programme under Grant Agreement No. 765998.

Author ORCIDs.
Thomas Indlekofer https://orcid.org/0000-0002-3090-978X;
Abel Faure-Beaulieu https://orcid.org/0000-0003-1535-6459;
James R. Dawson https://orcid.org/0000-0002-3069-6948;
Nicolas Noiray https://orcid.org/0000-0003-3362-9721.

Appendix A. Calibration of the model parameters

In this appendix, we explain how the parameters of the model, given by (3.1) and (3.2), are identified from the experimental data. To that end, we make use of the Langevin equation (4.1), which was obtained by applying spatio-temporal averaging to (3.1), as it was done by Faure-Beaulieu & Noiray (2020). As in Faure-Beaulieu *et al.* (2021*a*), we decouple equations for A and χ in the system (4.1), by using the mean values of A, $|\chi|$ and θ, which gives

$$\dot{A} = \left(\nu + \frac{c_2\beta}{4}\cos(2(\theta_0 - \Theta_\beta))\cos(2\chi_0)\right)A - \frac{3\kappa}{64}(5 + \cos(4\chi_0))A^3 + \frac{3\Gamma}{4\omega^2 A} + \zeta_A, \tag{A1}$$

$$\dot{\chi} = \frac{3\kappa}{64}A_0^2\sin(4\chi) - \frac{c_2\beta}{4}\cos(2(\theta_0 - \Theta_\beta))\sin(2\chi) - \frac{\Gamma\tan(2\chi)}{2\omega^2 A_0^2} + \frac{1}{A_0}\zeta_\chi, \tag{A2}$$

with A_0, χ_0 and θ_0 the average values of A, $|\chi|$ and θ (mod π). By considering such simplification of the model, the data post-processing is significantly eased without compromising the accuracy of the identified parameters. Indeed, using the parameters identified on the basis of these decoupled equations leads to model simulations that are in close agreement with the experiments. This is because the relative fluctuations of A, and of the terms involving χ and θ are small. Equation (4.5) implies that θ is attracted towards Θ_β, so that $\theta_0 - \Theta_\beta$ is replaced by 0 in (A1) and (A2), and the parameter Θ_β

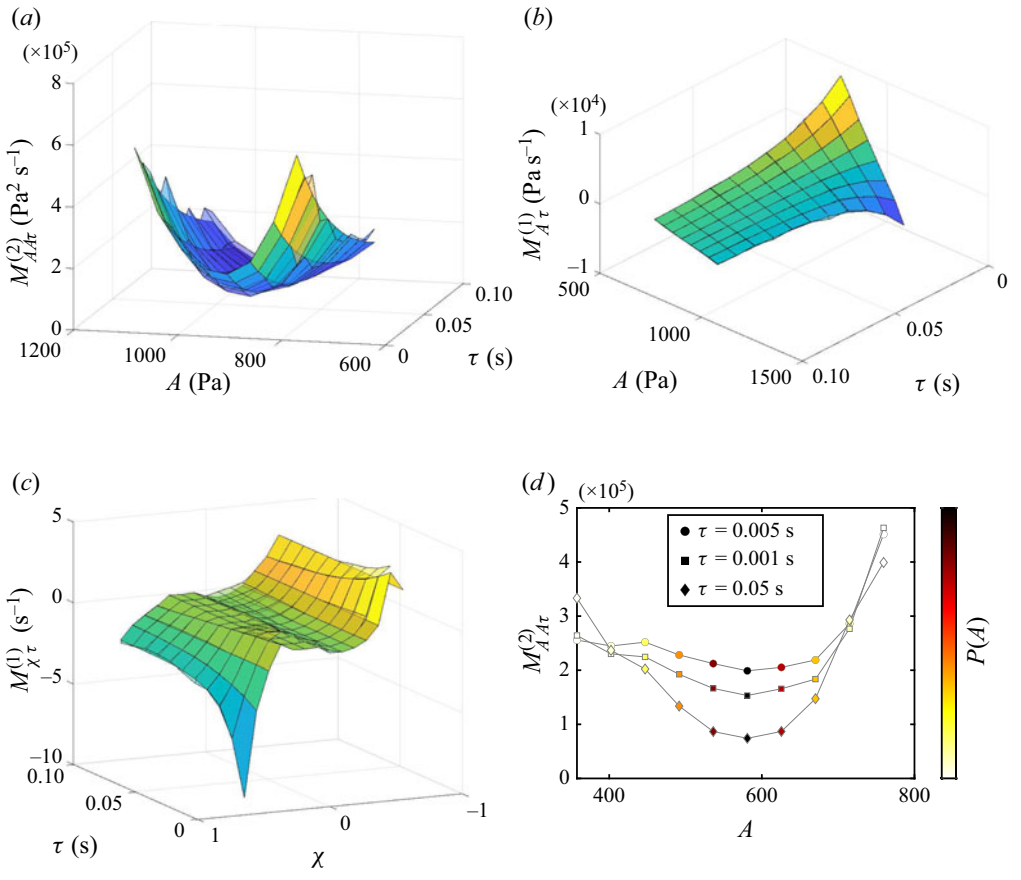

Figure 12. (*a–c*) Transition moments of $A(t)$ and $\chi(t)$ for $\Phi = 0.55$. For the extrapolation $\tau \to 0$, interpolated exponential functions of τ for each amplitude and nature angle are used, and the associated surface is superimposed in these figures on the raw transition moments. (*d*) Shows the extrapolation of the second transition moment of $A(t)$ for a non-filtered simulation, allowing a smaller time step than in the experiment. It reveals that the surface flattens when $\tau \to 0$. Darker colour shades correspond to higher probabilities of A. (*a*) Second transition moment of $A(t)$, (*b*) first transition moment of $A(t)$, (*c*) first transition moment of $\chi(t)$ and (*d*) second transition moment of A(t) (simulation).

is associated with the peak value of $P(\theta)$. The decoupled equations can be written in the following compact form:

$$\dot{A} = F_A(A) + \sqrt{D_{AA}}\zeta_1, \tag{A3}$$

$$\dot{\chi} = F_\chi(\chi) + \sqrt{D_{\chi\chi}}\zeta_2, \tag{A4}$$

where $\zeta_{1,2}$ are Gaussian white noises, i.e. $\langle \zeta_i(t) \rangle = 0$ and $\langle \zeta_i(t)\zeta_i(t+\tau) \rangle = \delta(\tau)$, and where $D_{AA} = \Gamma/(2\omega^2)$ and $D_{\chi\chi} = \Gamma/(2\omega^2 A_0^2)$. Each of the Langevin equations (A3) and (A4) has an equivalent FPE. They govern the time evolution of the PDF of A and χ, and their drift and diffusion coefficients are respectively F_A and F_χ, and D_{AA} and $D_{\chi\chi}$. Experimental data are used to identify the model parameters ν, $c_2\beta$, κ and Γ, with a method based on the extraction of these drift and diffusion coefficients the FPEs from time traces (Friedrich *et al.* 2011).

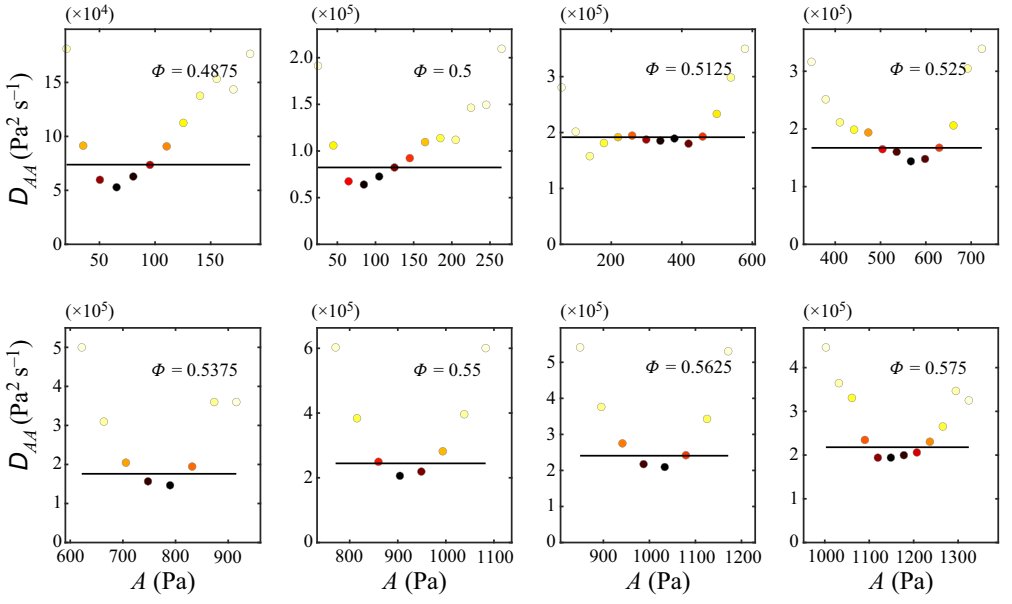

Figure 13. Fitting of $D_{AA} = \Gamma/(2\omega^2)$ using $\lim_{\tau\to 0} M^{(2)}_{AA\tau}$ weighted by $P(A)$, the latter defining the colour of the dots.

The drift and diffusion coefficients of FPEs are equal to the limit of the first two transition moments. Therefore, F_A and F_χ, which govern the deterministic part of the stochastic processes $A(t)$ and $\chi(t)$, are obtained by computing the first-order moments of these time series

$$F_A(A) = \lim_{\tau\to 0} \frac{1}{\tau} \int (\check{A} - A) P(\check{A}, t+\tau | A, t)\, \mathrm{d}\check{A} \equiv \lim_{\tau\to 0} M^{(1)}_{A\tau}, \tag{A5}$$

$$F_\chi(\chi) = \lim_{\tau\to 0} \frac{1}{\tau} \int (\check{\chi} - \chi) P(\check{\chi}, t+\tau | \chi, t)\, \mathrm{d}\check{\chi} \equiv \lim_{\tau\to 0} M^{(1)}_{\chi\tau}, \tag{A6}$$

and the noise intensity in the equation for $A(t)$ is obtained with the second-order moment

$$D_{AA} = \lim_{\tau\to 0} \frac{1}{\tau} \int (\check{A} - A)^2 P(\check{A}, t+\tau | A, t)\, \mathrm{d}\check{A} \equiv \lim_{\tau\to 0} M^{(2)}_{AA\tau}. \tag{A7}$$

In these integrals, the conditional probability density $P(\check{y}, t+\tau | y, t)$ defines the probability that the variable takes the value $\check{y}$ at a time $t+\tau$, knowing that it was at y at the time t. This identification method has been applied to thermoacoustic and aeroacoustic problems, e.g. Noiray & Denisov (2017) and Boujo *et al.* (2020), and the latter reference contains a detailed discussion about its applicability to the problem at hand.

Considering that the model describes the stochastic dynamics of a single thermoacoustic eigenmode of the annular combustor, the parameter identification method is only applicable if the frequency content associated with the eigenmode of interest is isolated. This is achieved by band-pass filtering the time series around the thermoacoustic peak. The width of the rectangular band-pass filter is $\Delta f = 100$ Hz. As explained in Boujo & Noiray (2017), due to the filtering of the signal, only the statistics extracted for $\tau > 1/\Delta f$ are meaningful. To obtain the limits for $\tau \to 0$ in (A5) and (A6), an extrapolation is then performed with exponential functions $a_1 \exp(a_2\tau) + a_3$ whose coefficients are obtained

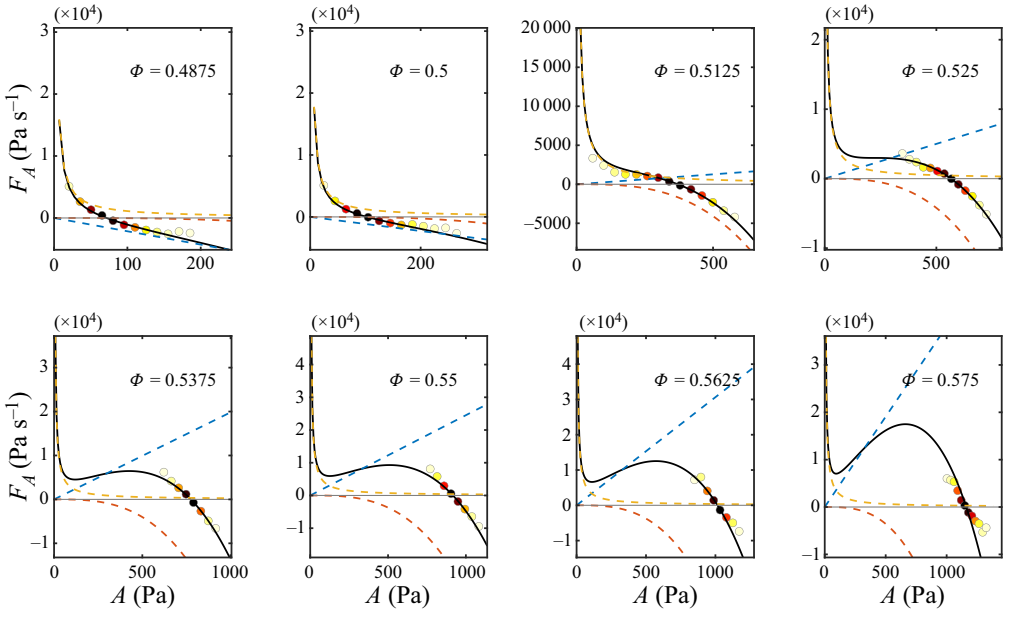

Figure 14. Fitting of $F_A(A)$ using $\lim_{\tau\to 0} M^{(1)}_{A\tau}$ weighted by $P(A)$, the latter defining the colour of the dots.

with least square fitting. The interested reader can also refer to the recent work of Bonciolini *et al.* (2017) and Lehle & Peinke (2018) for the analysis of stochastic processes driven by Ornstein–Uhlenbeck noise. An example of the extrapolations performed in the present work is shown in figure 12 for $\Phi = 0.55$. The next step is to fit the model to these extrapolated time limits of the transition moments. The order in which the parameters are identified for each Φ is the following.

First, the noise intensity Γ is obtained by taking the average of D_{AA} weighted with the PDF of A. This gives access to the value of Γ/ω^2 and therefore to Γ since $\omega = 2\pi f$ is directly obtained from the acoustic spectrum. This first step of the parameter identification is shown in figure 13. As already observed in previous studies using the same model-based parameter identification method for self-sustained oscillators (e.g. Noiray & Denisov 2017), the extrapolated values of $D_{AA}(A)$ exhibit a curved dependence with respect to A, which seems contradictory with the expected amplitude-independent transition-moment limit of the assumed model with additive white noise in (A1). Actually, this parabolic-like shape results from difficulties in reliably extrapolating the finite-time second transition moment of the amplitude to its limit at $\tau \to 0$, because it is computed from the amplitude time traces of band-pass filtered, and thus smoothed, experimental acoustic data. Indeed, using synthetic data generated by simulating (5.2), the finite-time transition moment $M^{(2)}_{AA\tau}$ can be more reliably obtained for smaller transition times τ than for the band-pass filtered experimental data and one retrieves in figure 12(*d*) the expected flattening of $M^{(2)}_{AA\tau}$ for $\tau \to 0$.

Second, knowing ω and Γ, we identify the parameters C_1 and C_2 of the function

$$C_1 A + C_2 A^3 + \frac{3\Gamma}{4\omega^2 A}, \tag{A8}$$

which provide the best fit with $F_A(A)$. This step is shown in figure 14, where a simple least squares approach is used with a weighting of F_A with $P(A)$. Then, considering (A1),

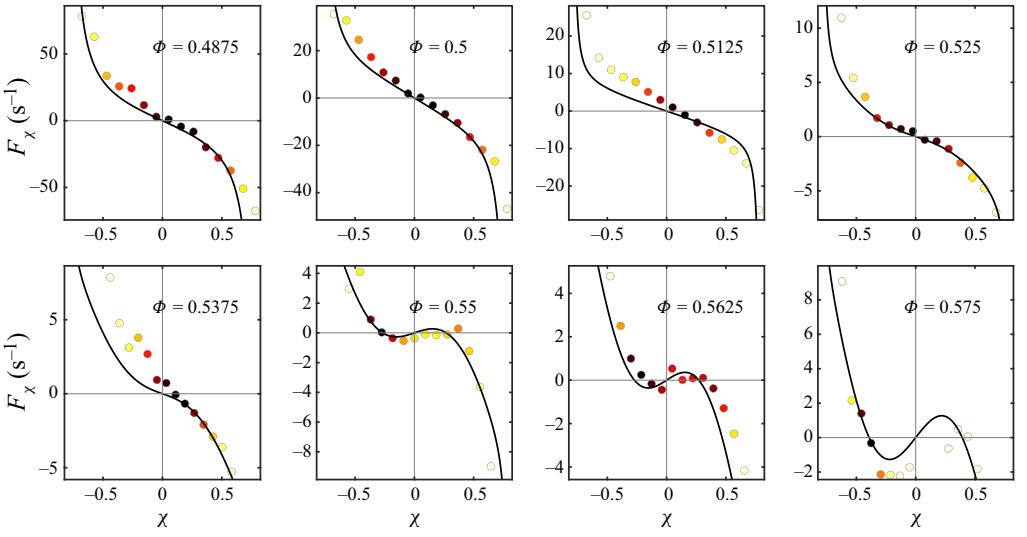

Figure 15. Fitting of $F_\chi(\chi)$ using $\lim_{\tau\to 0} M^{(1)}_{\chi\tau}$ weighted by $[P(\chi)]^2$, the latter defining the colour of the dots.

we know that $C_1 = \nu + c_2\beta/4\cos(2\chi_0)$ and $C_2 = -3\kappa(5+\cos(4\chi_0))/64$. Therefore, we obtain κ and the coefficient $C_1 = \nu + c_2\beta/4\cos(2\chi_0)$. It is found that the identified κ does not significantly change when Φ is varied between 0.5 and 0.55, with a value around 1.2×10^{-4} Pa^{-2} s^{-1}. To finally identify $c_2\beta$ and ν, we proceed to a last fit by considering (A2) and its associated F_χ. The fitted function is

$$3\kappa A_0^2\sin(4\chi) + C_3\sin(2\chi) - \frac{\Gamma\tan(2\chi)}{2\omega^2 A_0^2}, \tag{A9}$$

and the fitting outcome is shown in figure 15. The weighting used here is $[P(\chi)]^2$. Here, the only coefficient to identify is C_3, which is equal to $-c_2\beta/4$ in the model. The method does not permit separate identification of c_2 and β, but only the value of the lumped parameter $c_2\beta$. With this, all the parameters are identified. Linear regressions of the model parameters $\nu(\Phi)$, $\{c_2\beta\}(\Phi)$ and $\{\Gamma/\omega^2\}(\Phi)$ are presented in figure 9 and used in the model.

References

Acharya, V., Aguilar, M., Malanosk, M. & Lieuwen, T. 2014 Dynamics of a transversely excited swirling, lifted flame: flame response modeling and comparison with experiments. *Trans. ASME J. Engng Gas Turbines Power* **136** (5), 051503.

Aerts, C. 2021 Probing the interior physics of stars through asteroseismology. *Rev. Mod. Phys.* **93** (1), 015001.

Aguilar, J.G., Dawson, J.R., Schuller, T., Durox, D., Prieur, K. & Candel, S. 2021 Locking of azimuthal modes by breaking the symmetry in annular combustors. *Combust. Flame* **234**, 111639.

Bauerheim, M., Cazalens, M. & Poinsot, T. 2015 A theoretical study of mean azimuthal flow and asymmetry effects on thermo-acoustic modes in annular combustors. *Proc. Combust. Inst.* **35** (3), 3219–3227.

Bauerheim, M., Nicoud, F. & Poinsot, T. 2016 Progress in analytical methods to predict and control azimuthal combustion instability modes in annular chambers. *Phys. Fluids* **28** (2), 021303.

Bauerheim, M., Salas, P., Nicoud, F. & Poinsot, T. 2014 Symmetry breaking of azimuthal thermo-acoustic modes in annular cavities: a theoretical study. *J. Fluid Mech.* **760**, 431–465.

BERGER, F.M., HUMMEL, T., HERTWECK, M., KAUFMANN, J., SCHUERMANS, B. & SATTELMAYER, T. 2017 High-frequency thermoacoustic modulation mechanisms in swirl-stabilized gas turbine combustors-part I: experimental investigation of local flame response. *Trans. ASME J. Engng Gas Turbines Power* **139** (7), 071501.

BERGER, F.M., HUMMEL, T., SCHUERMANS, B. & SATTELMAYER, T. 2018 Pulsation-amplitude-dependent flame dynamics of high-frequency thermoacoustic oscillations in lean-premixed gas turbine combustors. *Trans. ASME J. Engng Gas Turbines Power* **140** (4), 041507.

BONCIOLINI, G., BOUJO, E. & NOIRAY, N. 2017 Output-only parameter identification of a colored-noise-driven van-der-pol oscillator: thermoacoustic instabilities as an example. *Phys. Rev.* E **95** (6), 062217.

BONCIOLINI, G., FAURE BEAULIEU, A., BOURQUARD, C. & NOIRAY, N. 2021 Low order modelling of thermoacoustic instabilities and intermittency: flame response delay and nonlinearity. *Combust. Flame* **226**, 396–411.

BÖTTCHER, F., PEINKE, J., KLEINHANS, D., FRIEDRICH, R., LIND, P.G. & HAASES, M. 2006 Reconstruction of complex dynamical systems affected by strong measurement noise. *Phys. Rev. Lett.* **97** (9), 090603.

BOUJO, E., BOURQUARD, C., XIONG, Y. & NOIRAY, N. 2020 Processing time-series of randomly forced self-oscillators: the example of beer bottle whistling. *J. Sound Vib.* **464**, 114981.

BOUJO, E. & NOIRAY, N. 2017 Robust identification of harmonic oscillators parameters using the adjoint fokker-planck equation. *Proc. R. Soc.* A **473** (2200), 20160894.

BOURGOUIN, J.F., DUROX, D., MOECK, J.P., SCHULLER, T. & CANDEL, S. 2015*a* Characterization and modeling of a spinning thermoacoustic instability in an annular combustor equipped with multiple matrix injectors. *Trans. ASME J. Engng Gas Turbines Power* **137** (2), 021503.

BOURGOUIN, J.F., DUROX, D., MOECK, J.P., SCHULLER, T. & CANDEL, S. 2015*b* A new pattern of instability observed in an annular combustor: the slanted mode. *Proc. Combust. Inst.* **35** (3), 3237–3244.

BRÜCKNER, D.B., RONCERAY, P. & BROEDERSZ, C.P. 2020 Inferring the dynamics of underdamped stochastic systems. *Phys. Rev. Lett.* **125** (5), 058103.

BUSCHMANN, P.E., MENSAH, G.A. & MOECK, J.P. 2020 Intrinsic thermoacoustic modes in an annular combustion chamber. *Combust. Flame* **214**, 251–262.

CALLAHAM, J.L., LOISEAU, J.-C., RIGAS, G. & BRUNTON, S.L. 2021 Nonlinear stochastic modelling with langevin regression. *Proc. R. Soc.* A **477** (2250), 20210092.

CHTEREV, I., *et al.* 2014 Flame and flow topologies in an annular swirling flow. *Combust Sci. Technol* **186** (8), 1041–1074.

CLAVIN, P., KIM, J.S. & WILLIAMS, F.A. 1994 Turbulence-induced noise effects on high-frequency combustion instabilities. *Combust Sci. Technol.* **96** (1-3), 61–84.

CRAWFORD, J.D. & KNOBLOCH, E. 1991 Symmetry and symmetry-breaking bifurcations in fluid dynamics. *Annu. Rev. Fluid Mech.* **23** (1), 341–387.

DAWSON, J.R. & WORTH, N.A. 2013 The effect of baffles on self-excited azimuthal modes in an annular combustor. *Proc. Combust. Inst.* **35** (3), 3283–3290.

EVESQUE, S., POLIFKE, W. & PANKIEWITZ, C. 2003 Spinning and azimuthally standing acoustic modes in annular combustors. In *AIAA/CEAS Aeroacoustics Conference*, vol. 9. *AIAA Paper* 2003-3182.

FANG, Y., YANG, Y., HU, K., WANG, G., LI, J. & ZHENG, Y. 2021 Experimental study on self-excited thermoacoustic instabilities and intermittent switching of azimuthal and longitudinal modes in an annular combustor. *Phys. Fluids* **33** (8), 084104.

FARANDA, D., SATO, Y., SAINT-MICHEL, B., WIERTEL, C., PADILLA, V., DUBRULLE, B. & DAVIAUD, F. 2017 Stochastic chaos in a turbulent swirling flow. *Phys. Rev. Lett.* **119** (1), 014502.

FAURE-BEAULIEU, A., INDLEKOFER, T., DAWSON, J. & NOIRAY, N. 2021*a* Experiments and low-order modelling of intermittent transitions between clockwise and anticlockwise spinning thermoacoustic modes in annular combustors. *Proc. Combust. Inst.* **38** (4), 5943–5951.

FAURE-BEAULIEU, A., INDLEKOFER, T., DAWSON, J.R. & NOIRAY, N. 2021*b* Imperfect symmetry of real annular combustors: beating thermoacoustic modes and heteroclinic orbits. *J. Fluid Mech.* **925**, R1.

FAURE-BEAULIEU, A. & NOIRAY, N. 2020 Symmetry breaking of azimuthal waves: slow-flow dynamics on the bloch sphere. *Phys. Rev. Fluids* **5** (2), 023201.

FERRETTI, F., CHARDÈS, V., MORA, T., WALCZAK, A.M. & GIARDINA, I. 2020 Building general langevin models from discrete datasets. *Phys. Rev.* X **10** (3), 031018.

FLEURY, R., SOUNAS, D.L., SIECK, C.F., HABERMAN, M.R. & ALÙ, A. 2014 Sound isolation and giant linear nonreciprocity in a compact acoustic circulator. *Science* **343** (6170), 516–519.

FOURNIER, G.J.J., HAERINGER, M., SILVA, C.F. & POLIFKE, W. 2021 Low-order modeling to investigate clusters of intrinsic thermoacoustic modes in annular combustors. *Trans. ASME J. Engng Gas Turbines Power* **143**, 041025.

FRIEDRICH, R., PEINKE, J., SAHIMI, M. & REZA RAHIMI TABAR, M. 2011 Approaching complexity by stochastic methods: from biological systems to turbulence. *Phys. Rep.* **506** (5), 87–162.

FRIEDRICH, R., RENNER, C., SIEFERT, M. & PEINKE, J. 2002 Comment on "Indispensable finite time corrections for fokker-Planck equations from time series data". *Phys. Rev. Lett.* **89** (14), 149401.

FRISHMAN, A. & RONCERAY, P. 2020 Learning force fields from stochastic trajectories. *Phys. Rev.* X **10** (2), 021009.

GHIRARDO, G. & BOTHIEN, M.R. 2018 Quaternion structure of azimuthal instabilities. *Phys. Rev. Fluids* **3** (11), 113202.

GHIRARDO, G. & GANT, F. 2021 Averaging of thermoacoustic azimuthal instabilities. *J. Sound Vib.* **490**, 115732.

GHIRARDO, G. & JUNIPER, M.P. 2013 Azimuthal instabilities in annular combustors: standing and spinning modes. *Proc. R. Soc.* A **469** (2157), 20130232.

GHIRARDO, G., JUNIPER, M.P. & MOECK, J.P. 2016 Weakly nonlinear analysis of thermoacoustic instabilities in annular combustors. *J. Fluid Mech.* **805**, 52–87.

GHIRARDO, G., NYGÅRD, H.T., CUQUEL, A. & WORTH, N.A. 2021 Symmetry breaking modelling for azimuthal combustion dynamics. *Proc. Combust. Inst.* **38**, 5953–5962.

GOPALAKRISHNAN, E.A., TONY, J., SREELEKHA, E. & SUJITH, R.I. 2016 Stochastic bifurcations in a prototypical thermoacoustic system. *Phys. Rev.* E **94** (2), 022203.

HUMBERT, S.C., MOECK, J., ORCHINI, A. & PASCHEREIT, C.O. 2021 Effect of an azimuthal mean flow on the structure and stability of thermoacoustic modes in an annular combustor model with electroacoustic feedback. *Trans. ASME J. Engng Gas Turbines Power* **143**, 061026.

HUMMEL, T., BERGER, F., HERTWECK, M., SCHUERMANS, B. & SATTELMAYER, T. 2017 High-frequency thermoacoustic modulation mechanisms in swirl-stabilized gas turbine combustors-part II: modeling and analysis. *Trans. ASME J. Engng Gas Turbines Power* **139** (7), 071502.

HUMMEL, T., BERGER, F., STADLMAIR, N., SCHUERMANS, B. & SATTELMAYER, T. 2018 Extraction of linear growth and damping rates of high-frequency thermoacoustic oscillations from time domain data. *Trans. ASME J. Engng Gas Turbines Power* **140** (5), 051505.

INDLEKOFER, T., FAURE-BEAULIEU, A., NOIRAY, N. & DAWSON, J. 2021 The effect of dynamic operating conditions on the thermoacoustic response of hydrogen rich flames in an annular combustor. *Combust. Flame* **223**, 284–294.

JUEL, A., DARBYSHIRE, A.G. & MULLIN, T. 1997 The effect of noise on pitchfork and hopf bifurcations. *Proc. R. Soc.* A **453** (1967), 2627–2647.

KIM, J.-W., GILLMAN, W., EMERSON, B., WU, D., JOHN, T., ACHARYA, V., ISONO, M., SAITOH, T. & LIEUWEN, T. 2021 Modal dynamics of high-frequency transverse combustion instabilities. *Proc. Combust. Inst.* **38**, 6155–6163.

KIM, J., JOHN, T., ADHIKARI, S., WU, D., EMERSON, B., ACHARYA, V., ISONO, M., SAITO, T. & LIEUWEN, T. 2022 Nonlinear dynamics of combustor azimuthal modes: experiments and modeling. *Combust. Flame* **238**, 111931.

KREBS, W., FLOHR, P., PRADE, B. & HOFFMANN, S. 2002 Thermoacoustic stability chart for high intensity gas turbine combustion system. *Combust. Sci. Technol.* **174** (7), 99–128.

LAURENT, C., BADHE, A. & NICOUD, F. 2021 Representing the geometrical complexity of liners and boundaries in low-order modeling for thermoacoustic instabilities. *J. Comput. Phys.* **428**, 110077.

LEE, M., KIM, K.T., GUPTA, V. & LI, L.K.B. 2021 System identification and early warning detection of thermoacoustic oscillations in a turbulent combustor using its noise-induced dynamics. *Proc. Combust. Inst.* **38**, 6025–6033.

LEE, M., ZHU, Y., LI, L.K.B. & GUPTA, V. 2019 System identification of a low-density jet via its noise-induced dynamics. *J. Fluid Mech.* **862**, 200–215.

LEHLE, B. & PEINKE, J. 2018 Analyzing a stochastic process driven by ornstein-uhlenbeck noise. *Phys. Rev.* E **97** (1), 012113.

LI, J., MORGANS, A.S. & YANG, L. 2020*a* The three-dimensional acoustic field in cylindrical and annular ducts with an axially varying mean temperature. *Aerosp. Sci. Technol.* **99**, 105712.

LI, X., WANG, Y., WANG, N. & ZHAO, D. 2020*b* Stochastic properties of thermoacoustic oscillations in an annular gas turbine combustion chamber driven by colored noise. *J. Sound Vib.* **480**, 115423.

LI, C., YANG, D., LI, S. & ZHU, M. 2019 An analytical study of the effect of flame response to simultaneous axial and transverse perturbations on azimuthal thermoacoustic modes in annular combustors. *Proc. Combust. Inst.* **37** (4), 5279–5287.

LIEUWEN, T.C. 2003 Statistical characteristics of pressure oscillations in a premixed combustor. *J. Sound Vib.* **260** (1), 3–17.

LIEUWEN, T.C. 2012 *Unsteady Combustor Physics*. Cambridge University Press.

LIEUWEN, T. & BANASZUK, A. 2005 Background noise effects on combustor stability. *J. Propul. Power* **21** (1), 25–31.

LÓPEZ-CABALLERO, M. & BURGUETE, J. 2013 Inverse cascades sustained by the transfer rate of angular momentum in a 3d turbulent flow. *Phys. Rev. Lett.* **110**, 124501.

MAGRI, L., BAUERHEIM, M., NICOUD, F. & JUNIPER, M.P. 2016 Stability analysis of thermo-acoustic nonlinear eigenproblems in annular combustors. Part II. Uncertainty quantification. *J. Comput. Phys.* **325**, 411–421.

MARTI, G.E., OLF, R. & STAMPER-KURN, D.M. 2015 Collective excitation interferometry with a toroidal bose-einstein condensate. *Phys. Rev.* A **91** (1), 013602.

MEGYERI, B., HARVIE, G., LAMPIS, A. & GOLDWIN, J. 2018 Directional bistability and nonreciprocal lasing with cold atoms in a ring cavity. *Phys. Rev. Lett.* **121** (16), 163603.

MENSAH, G.A., MAGRI, L., ORCHINI, A. & MOECK, J.P. 2019 Effects of asymmetry on thermoacoustic modes in annular combustors: a higher-order perturbation study. *Trans. ASME J. Engng Gas Turbines Power* **141**, 041030.

MOECK, J.P., DUROX, D., SCHULLER, T. & CANDEL, S. 2019 Nonlinear thermoacoustic mode synchronization in annular combustors. *Proc. Combust. Inst.* **37** (4), 5343–5350.

MORGANS, A.S. & STOW, S.R. 2007 Model-based control of combustion instabilities in annular combustors. *Combust. Flame* **150**, 380–399.

NOIRAY, N. 2017 Linear growth rate estimation from dynamics and statistics of acoustic signal envelope in turbulent combustors. *Trans. ASME J. Engng Gas Turbines Power* **139** (4), 041503.

NOIRAY, N., BOTHIEN, M. & SCHUERMANS, B. 2011 Analytical and numerical analysis of staging concepts in annular gas turbines. *Combust. Theor. Model.* **15** (5), 585–606.

NOIRAY, N. & DENISOV, A. 2017 A method to identify thermoacoustic growth rates in combsution chambers from dynamic pressure time series. *Proc. Combust. Inst.* **36** (3), 3843–3850.

NOIRAY, N. & SCHUERMANS, B. 2013*a* Deterministic quantities characterizing noise driven hopf bifurcations in gas turbine combustors. *Intl J. Non-Linear Mech.* **50**, 152–163.

NOIRAY, N. & SCHUERMANS, B. 2013*b* On the dynamic nature of azimuthal thermoacoustic modes in annular gas turbine combustion chambers. *Proc. R. Soc.* A **469** (2151), 20120535.

NYGÅRD, H.T., MAZUR, M., DAWSON, J.R. & WORTH, N.A. 2019 Flame dynamics of azimuthal forced spinning and standing modes in an annular combustor. *Proc. Combust. Inst.* **37**, 5113–5120.

O'CONNOR, J. & LIEUWEN, T. 2011 Disturbance field characteristics of a transversely excited burner. *Combust. Sci. Technol.* **183** (5), 427–443.

ORCHINI, A., MENSAH, G.A. & MOECK, J.P. 2019 Effects of nonlinear modal interactions on the thermoacoustic stability of annular combustors. *Trans. ASME J. Engng Gas Turbines Power* **141** (2), 021002.

PÉTRÉLIS, F., FAUVE, S., DORMY, E. & VALET, J.P. 2009 Simple mechanism for reversals of earth's magnetic field. *Phys. Rev. Lett.* **102**, 144503.

POINSOT, T. 2017 Prediction and control of combustion instabilities in real engines. *Proc. Combust. Inst.* **36** (1), 1–28.

PRIEUR, K., DUROX, D., SCHULLER, T. & CANDEL, S. 2017 A hysteresis phenomenon leading to spinning or standing azimuthal instabilities in an annular combustor. *Combust. Flame* **175**, 283–291.

RAYLEIGH, J.L. 1878 The explanation of certain acoustical phenomena. *Nature* **18** (455), 319–321.

RICE, J.E., *et al.* 2011 Rotation reversal bifurcation and energy confinement saturation in tokamak ohmic l-mode plasmas. *Phys. Rev. Lett.* **107** (26), 265001.

SAURABH, A. & PASCHEREIT, C.O. 2017 Dynamics of premixed swirl flames under the influence of transverse acoustic fluctuations. *Combust. Flame* **182**, 298–312.

SCHUERMANS, B., PASCHEREIT, C.O. & MONKEWITZ, P. 2006 Non linear combustion instabilities in annular gas turbine combustors. In *AIAA Aerospace Sciences Meeting and Exhibit*, vol. 44th. *AIAA Paper* 2006-0549.

SEUME, J.R., VORTMEYER, N., KRAUSE, W., HERMANN, J., HANTSCHK, C.-C., ZANGL, P., GLEIS, S., VORTMEYER, D. & ORTHMANN, A. 1998 Application of active combustion instability control to a heavy duty gas turbine. *Trans. ASME J. Engng Gas Turbines Power* **120** (4), 721–726.

SHEN, Z., ZHANG, Y.-L., CHEN, Y., ZOU, C.-L., XIAO, Y.-F., ZOU, X.-B., SUN, F.-W., GUO, G.-C. & DONG, C.-H. 2016 Experimental realization of optomechanically induced non-reciprocity. *Nat. Photonics* **10** (10), 657–661.

SIEBER, M., PASCHEREIT, C.O. & OBERLEITHNER, K. 2021 Stochastic modelling of a noise-driven global instability in a turbulent swirling jet. *J. Fluid Mech.* **916**, A7.

SIEGERT, S., FRIEDRICH, R. & PEINKE, J. 1998 Analysis of data sets of stochastic systems. *Phys. Lett.* A **243**, 275–280.

SINGH, S., ROY, A., REEJA, K.V., NAIR, A., CHAUDHURI, S. & SUJITH, R.I. 2021 Intermittency, secondary bifurcation and mixed-mode oscillations in a swirl-stabilized annular combustor: experiments and modeling. *Trans. ASME J. Engng Gas Turbines Power* **143** (5), 051028.

SMITH, T., EMERSON, B., PROSCIA, W. & LIEUWEN, T. 2018 Role of induced axial acoustics in transverse acoustic flame response. *Combust. Flame* **195**, 140–150.

WOLF, P., STAFFELBACH, G., GICQUEL, L.Y.M., MUELLER, J.-D. & POINSOT, T. 2012 Acoustic and large eddy simulation studies of azimuthal modes in annular combustion chambers. *Combust. Flame* **159** (11), 3398–3413.

WORTH, N. & DAWSON, J.R. 2013 Modal dynamics of self-excited azimuthal instabilities in an annular combustion chamber. *Combust. Flame* **160** (11), 2476–2489.

WORTH, N. & DAWSON, J.R. 2014 Flame dynamics and unsteady heat release rate of self-excited azimuthal modes in an annular combustor. *Combust. Flame* **161**, 2565–2578.

WORTH, N. & DAWSON, J.R. 2017 Effect of equivalence ratio on the modal dynamics of azimuthal combustion instabilities. *Proc. Combust. Inst.* **36** (3), 3743–3751.

YANG, D., LAERA, D. & MORGANS, A.S. 2019*a* A systematic study of nonlinear coupling of thermoacoustic modes in annular combustors. *J. Sound Vib.* **456**, 137–161.

YANG, D., SOGARO, F.M., MORGANS, A.S. & SCHMID, P.J. 2019*b* Optimising the acoustic damping of multiple helmholtz resonators attached to a thin annular duct. *J. Sound Vib.* **444**, 69–84.